The Astrophysical Journal, 719:1602–1618, 2010 August 20 doi:10.1088/0004-637X/719/2/1602

EQUILIBRIUM CONFIGURATIONS OF SYNCHRONOUS BINARIES: NUMERICAL SOLUTIONS AND APPLICATION TO KUIPER BELT BINARY 2001 QG_{298}

Orly Gnat[1,3] and Re'em Sari[1,2]
[1] Theoretical Astrophysics, California Institute of Technology, MC 350-17, Pasadena, CA 91125, USA; orlyg@tapir.caltech.edu
[2] Racah Institute of Physics, Hebrew University, Jerusalem 91904, Israel
Received 2010 March 29; accepted 2010 June 28; published 2010 August 2

ABSTRACT

We present numerical computations of the equilibrium configurations of tidally locked homogeneous binaries rotating in circular orbits. Unlike the classical Roche approximations, we self-consistently account for the tidal and rotational deformations of both components, and relax the assumptions of ellipsoidal configurations and Keplerian rotation. We find numerical solutions for mass ratios q between 10^{-3} and 1, starting at a small angular velocity for which tidal and rotational deformations are small, and following a sequence of increasing angular velocities. Each series terminates at an appropriate "Roche limit," above which no equilibrium solution can be found. Even though the Roche limit is crossed before the "Roche lobe" is filled, any further increase in the angular velocity will result in mass-loss. For close, comparable-mass binaries, we find that local deviations from ellipsoidal forms may be as large as 10%–20%, and departures from Keplerian rotation are significant. We compute the light curves that arise from our equilibrium configurations, assuming their distance is $\gg$1 AU (e.g., in the Kuiper Belt). We consider both backscatter (proportional to the projected area) and diffuse (Lambert) reflections. Backscatter reflection always yields two minima of equal depths. Diffuse reflection, which is sensitive to the surface curvature, generally gives rise to unequal minima. We find detectable intensity differences of up to 10% between our light curves and those arising from the Roche approximations. Finally, we apply our models to Kuiper Belt binary 2001 QG_{298}, and find a nearly edge-on binary with a mass ratio $q = 0.93^{+0.07}_{-0.03}$, angular velocity $\omega^2/G\rho = 0.333 \pm 0.001$ (statistical errors only), and pure diffuse reflection. For the observed period of 2001 QG_{298}, these parameters imply a bulk density $\rho = 0.72 \pm 0.04$ g cm^{-3}.

Key words: Kuiper Belt: general – Kuiper Belt objects: individual (2001 QG_{298}) – minor planets, asteroids: general

Online-only material: color figures

1. INTRODUCTION

The Kuiper Belt consists of a large number of small objects in heliocentric orbits beyond Neptune. The existence of the Kuiper Belt was suggested on theoretical grounds by Edgeworth (1943) and Kuiper (1951), but it was not until 1992 that the first Kuiper Belt object (KBO) was detected (Jewitt & Luu 1993). To date, more than 1000 KBOs are known. They are thought to be relics of the Sun's accretion disk and to hold signatures of the planetary migration process. Their physical properties, including their mass-distribution, compositions, and binary-fraction may thus hold the key to our understanding of the formation and evolution of the early solar system. A comprehensive review is provided by Luu & Jewitt (2002).

The properties of Kuiper Belt binaries place important constraints on theories of solar system evolution. In particular, the distributions of separations and mass ratios are a unique signature of the binary formation process. Over the past decade, more than 50 resolved Kuiper Belt binaries have been discovered and studied (Noll et al. 2008a, 2008b). These can be broadly divided into two groups (Noll et al. 2008b). The first consists of small satellites orbiting about larger KBOs. These systems are believed to have formed through a large collision, followed by tidal evolution, much like the Earth–Moon and Pluto–Charon systems (Hartmann & Davis 1975; Cameron & Ward 1976; McKinnon 1989). The second—more abundant—group, consists of comparable mass, large separation binaries. These are inconsistent with the classical formation mechanisms, and have prompted an abundance of new theoretical models (Weidenschilling 2002; Goldreich et al. 2002; Funato et al. 2004; Astakhov et al. 2005; Lee et al. 2007; Schlichting & Sari 2008; Perets & Naoz 2009; Gamboa Suárez et al. 2010; Naoz et al. 2010). Recently, Sheppard & Jewitt (2004) postulated the existence of a third group of Kuiper Belt binaries. By following the light curves of KBOs, they were able to identify an unresolved, comparable-mass small-separation binary-candidate, 2001 QB_{298}, based on its variability, photometric range, and period. Their analysis indicates that at least 10%–20% of all large KBOs may in fact be unresolved close-binary systems.

Our current interpretation of the observed light curves of KBOs relies on the classical theory of the equilibrium figures of rotation. The equilibrium configurations of rotating fluid bodies is a classical problem that was first investigated by Newton in the context of the figure of the Earth. Newton showed that the slow rotation of the Earth causes it to become a slightly oblate spheroid. In 1742, Maclaurin generalized the problem by relaxing the assumption of slow rotation. He derived a general relation between the velocity of rotation and the eccentricity of the resulting equilibrium spheroid. Maclaurin's relation implies that for any given angular velocity, two equilibrium solutions may be found, with different eccentricities. Decades later, Jacobi (1834) realized that triaxial ellipsoids are also possible equilibrium configurations of homogeneous rotating masses.

[3] Chandra Fellow.

The study of possible equilibrium configurations of binary systems was introduced by Roche (1847). Roche considered the equilibrium form of a satellite rotating about a rigid sphere in a circular Keplerian orbit. The satellite is deformed both by rotation and by the tides exerted by its spherical companion. A more accurate approach was later taken by Darwin (1906), who revisited the problem, allowing for mutual deformations of both bodies. Solutions to Darwin's problem may be found only in the limit of equal mass ratio ($q = 1$) or extreme mass ratio ($q \ll 1$). Both the Roche and Darwin solutions rely on the assumption that the equilibrium configurations are triaxial ellipsoids. A thorough review, analytic derivation, and stability analysis of these classical equilibrium configurations can be found in Chandrasekhar (1969).

In modern astrophysical research, these classical Roche ellipsoidal approximations are used in the study of a wide range of contact-binaries, including binaries in the solar system. Weidenschilling (1980) used equal-mass Darwin models to fit the observed light curves of asteroids 624 Hektor and 216 Kleopatra. In 1984, Leone et al. analytically constructed arbitrary mass-ratio Roche ellipsoidal models. When computing a Roche binary model for an arbitrary mass ratio, each component is in turn assumed to be spherical while the ellipsoidal configuration of its companion is calculated. Leone et al. (1984) used their theoretical photometric-range as a function of the angular velocity to constrain the mass ratios and densities of observed variable asteroids. Cellino et al. (1985) explicitly computed the light curves arising from the equilibrium Roche models of Leone et al., and compared them with an observed sample of asteroid light curves to constrain their orbital parameters and densities. Jewitt & Sheppard (2002) used the observed period and photometric range of KBO 20000 Varuna to consider possible (single) Jacobi ellipsoid and Roche binary models for this object. Takahashi & Ip (2004) computed the light curves arising from Roche ellipsoidal configurations to confirm the nature of the suspected binary KBO 2001 QG_{298}. Lacerda & Jewitt (2007) constructed a library of Jacobi-ellipsoid and Roche-binary light curves, and investigated the nature and densities of four variable KBOs (20000 Varuna, 2003 EL_{61}, 2001 QG_{298}, and 2000 GN_{171}) and of the Trojan asteroid 624 Hektor. Descamps (2008) applied Roche binary models to a sample of variable asteroids.

All of the binary models mentioned above rely on the assumptions of the Roche approximation, namely that each component is deformed by the tides of a *spherical* companion, and that the resulting configurations are ellipsoids rotating in Keplerian orbits. In this paper, we present new numerical computations of the equilibrium configurations of tidally locked homogeneous binaries orbiting in circular orbits. We self-consistently take into account the tidal and rotational deformations of *both* components, and relax the assumptions of ellipsoidal configurations and Keplerian rotation. For comparable-mass small-separation binaries, departures from ellipsoidal configurations and Keplerian rotation become significant.

Numerical solutions of the equilibrium configurations were previously computed for the cases of general mass ratio homogeneous binaries (Hachisu & Eriguchi 1984a) and for equal-mass polytropic binaries (Hachisu & Eriguchi 1984b). These works expanded the local gravitational potentials in terms of Legendre polynomials, which were used to approximate the potential on the surface of the two components. In our models we explicitly compute the local gravitational and rotational potentials on the surface of the two bodies, and use a Newton–Raphson-based scheme to converge to an equilibrium solution, for which the surface of each of the components is an equipotential surface. We then use our numerical solutions to calculate the light curves that these equilibrium configurations exhibit if placed in the Kuiper Belt, and demonstrate how these models can be used by fitting the observed light curve of Kuiper Belt binary 2001 QG_{298}.

In our computations we make several simplifying assumptions. First, we assume that the bodies' gravity dominates over their internal strength, so that they take the forms of rotating *fluid* binaries appropriate for their angular velocity. The ratio of the material rigidity to self-gravity determines a size scale above which bodies may be considered gravity dominated. For rigid monoliths, this size scale is $\sim 10^4$ km. However, many of the smaller solar system bodies are expected to be "rubble piles," for which the effective rigidity is reduced (Goldreich & Sari 2009 and references therein). Rubble piles larger than a few hundred kilometers are likely to be gravity dominated. In addition, over the age of the solar system, even smaller bodies will gradually take the forms dictated by gravity.

Second, we assume that the densities of the two binary components are equal. While this is likely the case for binaries formed through collisions, it is not necessarily true for binaries created via three-body interactions or due to dynamical friction. At the opposite extreme, when the density ratio is infinite, one of the bodies is effectively compressed into a point mass while the other takes a form similar to the classical Roche solution. These two limiting cases therefore span the range of possible configurations for different density-ratios.

Third, we assume that the binaries are tidally locked, so that their orbital and spin frequencies are equal, and their orbits circularized. If the orbital and spin velocities differ, the tidal bulge is carried ahead (or lags behind) the companion. Torques then act to re-align the system, inducing oscillations about the equilibrium aligned configuration. Internal dissipation damps these oscillations, and results in synchronized circular orbits. For the fiducial physical properties of large KBOs ($R \sim 100$ km, $\rho \sim 2$ g cm $^{-3}$, $k_{\rm rubble} \sim 10^{-3}$, $Q \sim 100$), such synchronization is expected to occur on time scales that are shorter than the age of the solar system for binaries forming with initial separations $\lesssim 50R$ (Goldreich & Sari 2009).

The outline of this paper is as follows. In Section 2, we briefly describe the numerical method that we use to compute the equilibrium configurations as a function of the mass ratio and angular velocity. Additional details are provided in Appendix A. In Section 3, we discuss the equilibrium figures of rotation. We first use analytic approximations to clarify the nature of the equilibrium solutions and the evolution surrounding the "Roche limit." We then present exact solutions for the equilibrium configurations using our numerical approach. In Section 4, we show that our equilibrium configurations are generally non-ellipsoidal, and deviate from pure Keplerian rotation. We explain how the angular momentum depends on the mass ratio, angular velocity, and tidal deformations. In Section 5 we compute the light curves that arise from the numerical configurations (the numerical procedure used to compute the light curves is described in Appendix B). We explain how the reflection properties of the materials affect the observed variability, and demonstrate the differences between our light curves and those resulting from the classical Roche approximations. Finally, in Section 6, we use our models to fit the observed properties of Kuiper Belt binary 2001 QG_{298}, and to derive the physical properties and bulk density of this system. We summarize our results in Section 7.

2. NUMERICAL METHOD

We are interested in finding the self-consistent equilibrium configuration of tidally-locked homogeneous binaries rotating in circular orbits. We assume that the bodies are strengthless, so that their equilibrium configurations are determined by the condition that the total (gravitational + rotational) potential is constant along the surface of each of the bodies (but may differ between the two bodies).

The parameters that determine the equilibrium configurations are the mass ratio $q \equiv M_2/M_1 < 1$, the separation between the components d, and the scaled angular velocity, $\omega^2/G\rho$. Here, we treat the separation and angular velocity as two independent parameters, and solve for the total mass of the system. For non-spherical configurations, the mass, separation, and angular velocity are not related via Kepler's law, and our choice of parameters allows us to conveniently explore the non-Keplerian nature of the solutions. Our numerical procedure is described in detail in Appendix A. We summarize the numerical scheme below.

We parameterize the surface of each body by specifying the distance from its center to the surface along N preset angular directions, $R_{i=1...N}$. We associate each of the N surface points with the small surface area surrounding it, and with a "mass cone" stretching from the center to this surface area. The mass in the i'th cone is then $M_i = \Delta\Omega\rho R_i^3/3$, where $\Delta\Omega$ is the solid angle that the cone occupies. We distribute the N points evenly, so that each cone covers an equal solid angle as viewed from the center of the body.

The potential at a point located on the surface is then the sum of the gravitational potential induced by the mass in all cones of both components, and the rotational potential about the common center of mass. For a model with N_1 points sampling the surface of M_1, and N_2 points sampling the surface of M_2, our goal is to solve for the $N_1 + N_2$ values of R_i for which the total potential along the surface of each body is constant. The value of the potential may differ between the two bodies.

We explicitly compute the gravitational and rotational potentials (see Appendix A). Our algorithm solves for $N_1 + N_2 + 2$ variables, namely the values of the distances R_i defining the surfaces of the bodies, and the values of the constant potentials along their surfaces, c_1 on M_1 and c_2 on M_2. The equations that we solve are the $N_1 + N_2$ conditions of constant potential, and the additional constrains provided by the given mass ratio q, and separation d,

$$\vec{F} \equiv \left\{ \begin{array}{l} \sum_{i\in M_1,M_2} V_i(\vec{R}_j) + V_{\rm rot}(\vec{R}_j) + c_k \quad , \quad {\rm for}\, j \in M_k \\ M_1/M_2 - q \\ x_{{\rm CoM},1} - x_{{\rm CoM},2} + d \end{array} \right\} = 0\,, \tag{1}$$

(see Appendix A), where $x_{{\rm CoM},k}$ is the center of mass position of M_k, along the direction separating the two components.

We use a Newton–Raphson scheme to solve for the variables $\vec{x} = (\vec{R}_j, c_1, c_2)$ that satisfy Equation (1). We start with an initial guess for the configurations, and in each iteration correct the current guess by a small amount $\vec{dx} = -\vec{F} \times \mathbf{J}^{-1}$, where $\mathbf{J}$ is the Jacobian derivatives matrix. We compute the Jacobian analytically, and iterate the Newton–Raphson scheme until the solution has converged so that $\vec{F} = 0$ to within some numerical threshold, and the correction $\vec{dx}$ is small compared to $\vec{x}$.

We define the $\hat{x}$-direction to be pointing from the more massive component to its companion, and the $\hat{z}$-direction to be parallel to the angular velocity vector. We assume that the equilibrium configurations have reflection symmetries about the $x-y$ and $x-z$ planes. We therefore distribute our N points on the surface of a quarter-sphere. In the discussion that follows, we use $\sim$1600 points on a quarter-sphere for each of the components.

3. EQUILIBRIUM FIGURES OF ROTATION

3.1. Physical Review and Analytic Approximations

In this section, we provide a brief introduction to the basic physical concepts underlying the derivation of equilibrium figures of rotations. We start by introducing the properties of single rotating Maclaurin spheroids. We then proceed to examine the properties of infinitesimal spheroids orbiting a massive companion. While the exact equilibrium configuration of a satellite may be far from spheroidal, this exercise captures the basic properties of the equilibrium figures of binary systems. We then proceed to examine triaxial ellipsoids. We write the equations for the single Jacobi ellipsoids, and then study infinitesimal triaxial ellipsoids satellites in binary systems.

In Section 3.2, we present our numerical results for the general equilibrium configuration of mutually deformed binaries. Our numerical configurations deviate from pure ellipsoidal forms. We discuss the properties of our solutions and compare them with the previous estimates based on the Roche ellipsoids in Section 4.

3.1.1. Maclaurin Spheroids

In his classical derivation of the rotational distortion of the Earth, Newton argued that since the Earth is in equilibrium, the weights of liquid filling two canals, one stretching from the center of the Earth to the equator, and the other from the center to the pole, must be equal. This is equivalent to demanding that the equator and the pole are a part of the same equipotential surface. Newton further pointed out that since the accelerations associated with both gravity and rotation are proportional to the distance from the center of the Earth, these weights (or, equivalently, the surface potentials measured relative to the center) are given by $0.5ha(h)$, where h is the height of the surface, and $a(h)$ is the acceleration on the surface.

When Maclaurin later addressed the general problem of spheroidal equilibrium configurations, he followed the arguments outlined by Newton. For the potentials on the equator and at the pole, we have

$$V_{\rm equator} = \frac{1}{2} a \times (g_{\rm equator} - \omega^2 a) \tag{2a}$$

$$V_{\rm pole} = \frac{1}{2} c \times g_{\rm pole} \tag{2b}$$

where $g_{\rm equator}$ is the gravitational acceleration on the equator, $g_{\rm pole}$ is the gravitational acceleration at the pole, ω is the angular velocity, a the semimajor axis ($a = b > c$) of the spheroid, $c = a\sqrt{1-e^2}$ is the semiminor axis, and e is the eccentricity.

For a spheroid, the gravitational acceleration along the equator and at the pole are analytical functions of the eccentricity e, and are given by (e.g., Chandrasekhar 1969),

$$g_{\rm equator} = 2\pi G\rho a \frac{\sqrt{1-e^2}}{e^3}\left(\sin^{-1} e - e\sqrt{1-e^2}\right), \tag{3a}$$

$$g_{\rm pole} = 4\pi G\rho a \frac{\sqrt{1-e^2}}{e^3}\left(e - \sqrt{1-e^2}\sin^{-1} e\right). \tag{3b}$$

Requiring the potentials on the equator and at the pole to be equal then yields,

$$\omega^2 = \frac{g_{\rm equator} - g_{\rm pole}\sqrt{1-e^2}}{a} = \pi G\rho \left[\frac{\sqrt{1-e^2}}{e^3} 2(3-2e^2)\sin^{-1} e - \frac{6}{e^2}(1-e^2) \right], \quad (4)$$

providing the relation between the eccentricity and angular velocity for Maclaurin spheroids.

3.1.2. An Illustrative Example: An Infinitesimal Spheroid in a Binary System

Let us now consider the problem of a binary system comprised of a massive primary of mass M orbited by an infinitesimal spheroidal ($a = b > c$) satellite. Here we assume that the system is tidally locked, so that the spin and orbital angular velocities are equal. For an infinitesimal satellite, the system's center of mass is effectively at the center of the massive primary, and we assume that the satellite is in a circular Keplerian orbit.

The massive primary exerts a tidal force on the spheroidal satellite. On the point facing the primary, this results in an acceleration opposing the satellites' own gravitational acceleration of magnitude $2GMa\,d^{-3}$, where d is the separation between the two components. On the polar axis, the primary serves to compress the secondary, providing an acceleration along the polar axis of $GMc\,d^{-3}$.

Following the previous line of argument, the potentials on the surface of the secondary can be readily computed. Writing V_a for the potential on the equatorial point facing the primary, and V_c for the polar potential,

$$V_a = \frac{1}{2}a\left(g_{\rm equator} - \omega^2 a - \frac{2GMa}{d^3}\right), \quad (5a)$$

$$V_c = \frac{1}{2}c\left(g_{\rm pole} + \frac{GM}{d^2}\frac{c}{d}\right) \quad (5b)$$

with $c = a\sqrt{1-e^2}$.

Demanding that these two potentials are equal, and assuming Keplerian rotation,

$$\frac{GM}{d^3} = \omega^2, \quad (6)$$

we now obtain

$$\omega^2 = \frac{g_{\rm equator} - g_{\rm pole}\sqrt{1-e^2}}{(4-e^2)a}, \quad (7)$$

which relates the eccentricity and rotational velocity of infinitesimal spheroids in binary systems. We note that the resulting spheroids are *not* genuine equilibrium configurations, because even for the eccentricities dictated by Equation (7), for which $V_a = V_c$, the value of the potential varies along the surface the spheroids.

Figure 1 shows the equatorial (V_a) and polar (V_c) potentials (relative to the satellite center, see Equations (5a) and (5b)), as functions of eccentricity for three representative values of the angular velocity. The solid curves show the equatorial potential, and the dashed curves show the polar potential. Equilibrium configurations arise where the two potentials obtain equal values and the curves cross. This is shown by the filled circles in Figure 1.

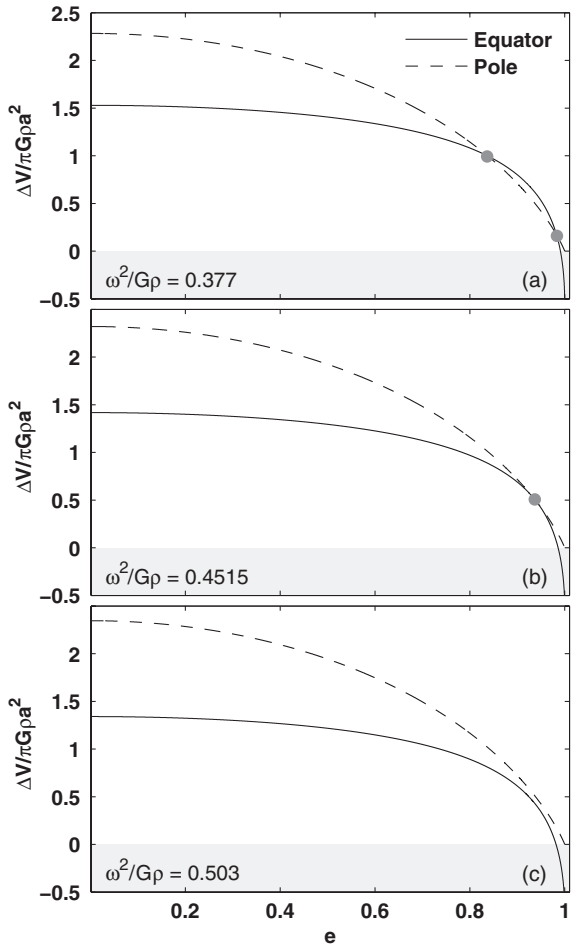

Figure 1. Equatorial (solid) and polar (dashed) potentials vs. eccentricity for an infinitesimal spheroid in a binary system. An equilibrium solution arises where the two curves cross (filled circles). The upper panel is for $\omega^2/G\rho = 0.377$, the middle is for the "Roche limit" spheroid (see the text) $\omega^2/G\rho = 0.4515$, and the lower panel is for $\omega^2/G\rho = 0.503$. In the shaded area ($\Delta V < 0$), the net force is away from the center.

For low angular velocities (panel (a)) there are two eccentricity solutions for a given angular velocity. The lower eccentricity solution is stable. A flattening of the equilibrium spheroid will result in restoring forces acting to raise the poles and compress the equator, and vice versa. The higher eccentricity solution is unstable. A flattening of the equilibrium spheroid will result in forces that act to flatten it even further, driving the eccentricity away from the equilibrium value. Figure 1 shows that the polar potential is always positive (relative to the satellite center), and the forces on the pole are therefore always directed toward the center. However, the equatorial potential on the point facing the primary becomes negative at large eccentricities, resulting in an outward force acting to unbind the material.

Panel (b) shows that there is a limiting angular velocity for which only one solution exists. This is known as the "Roche limit" configuration. For even higher angular velocities (panel (c)), the potential at the pole is higher than the potential at the equator for *any* eccentricity, and no equilibrium solution can be found.

Note that at the "Roche limit," the potential is still positive, and the material remains bound. The Roche limit is therefore crossed before the "Roche lobe"[4] is filled. For larger values of

[4] The Roche lobe is the region of space around a body within which a test particle is gravitationally bound to that body.

angular velocity, the force on the pole is *always* larger than the force on the equator (see panel (c)), and the configuration is therefore driven to an ever increasing eccentricity. Eventually, the potential on the equator will become negative, resulting in mass shedding along the equator. Even though the Roche limit occurs before the Roche lobe is filled, once the Roche limit is crossed the configuration will evolve to shed mass.

While our example assumed an unrealistic spheroidal configuration for the infinitesimal satellite, we find that it captures much of the physics at play in homogeneous binary systems. This includes the existence of two solutions, one of which is stable and the other not; the existence of a "Roche limit" that is reached before the Roche lobe is filled; and the understanding that despite this fact, beyond the Roche limit mass shedding will eventually occur. As we discuss below, the same principles apply for triaxial configurations.

3.1.3. Triaxial Ellipsoids: The Jacobi and Roche Solutions

Triaxial ellipsoids ($a > b > c$) are defined by two eccentricities, $e_1 = \sqrt{1-(b/a)^2}$ and $e_2 = \sqrt{1-(c/a)^2}$. To find the equilibrium configurations of single triaxial rotating ellipsoids, we demand that the surface potential along the three principal axes be equal. This provides two equations, which can be solved for the two eccentricities.

The gravitational accelerations along the principle axes of a triaxial ellipsoid are (e.g., Chandrasekhar 1969)

$$g_i = 2\pi G\rho A_i x_i, \tag{8}$$

where

$$A_i = a_1 a_2 a_3 \int_0^\infty \frac{du}{\left(a_i^2+u\right)\sqrt{\left(a_1^2+u\right)\left(a_2^2+u\right)\left(a_3^2+u\right)}}. \tag{9}$$

A comparison of the potential along the semimajor axis a, and the other equatorial axis b, yields

$$g_a - \omega^2 a = g_b\sqrt{1-e_1^2} - \omega^2 a\left(1-e_1^2\right), \tag{10}$$

whereas for the minor (polar) axis c,

$$g_a - \omega^2 a = g_c\sqrt{1-e_2^2}. \tag{11}$$

These two equations can be solved numerically for the values of e_1 and e_2 given an angular velocity ω. These solutions are the Jacobi ellipsoids.

If an infinitesimal triaxial ellipsoid is rotating about a massive spherical primary, the potential must be modified to include the tidal and gravitational contributions of the primary. In this case,

$$g_a - \omega^2 a - \frac{2GMa}{d^3} = g_b\sqrt{1-e_1^2} - \omega^2 a\left(1-e_1^2\right) + \frac{GMa}{d^3}\left(1-e_1^2\right), \tag{12}$$

and

$$g_a - \omega^2 a - \frac{2GMa}{d^3} = g_c\sqrt{1-e_2^2} + \frac{GMa}{d^3}\left(1-e_2^2\right). \tag{13}$$

Assuming Keplerian rotation (Equation (6)), we may express the above equations in terms of the eccentricities e_1 and e_2, and the angular velocity only,

$$\omega^2 = \frac{g_a - g_b\sqrt{1-e_1^2}}{3a}, \tag{14a}$$

$$\omega^2 = \frac{g_a - g_c\sqrt{1-e_2^2}}{\left(4-e_2^2\right)a}. \tag{14b}$$

These are the Roche ellipsoidal solutions for an extreme mass ratio ($q \ll 1$).

Figure 2 shows the Roche ellipsoid solutions for $q \ll 1$. Panel (a) shows the angular velocities given by Equations (14a) and (14b) (dark and gray contours) as functions of the eccentricities e_1 and e_2. Equilibrium solutions exist when the two equations yield equal values of angular velocity. Examples of equilibrium configurations are shown by the filled symbols. The circles correspond to $\omega^2/\pi G\rho = 0.06$, and the triangle to $\omega^2/\pi G\rho = 0.0901$.

Panel (b) shows the positions of the equilibrium solutions (solid curve). The dashed curve shows the line $e_1 = e_2$ (a prolate spheroid) for comparison. In panel (c), we display the angular velocity for which an equilibrium solution is found as a function of e_1. As in the case of the spheroidal satellite, for low angular velocities, two equilibrium solution are found (see filled circles). Panel (c) shows that there exists a maximal value of angular velocity for which only one solution can be found. This is the "Roche limit" ellipsoid, occurring at $\omega^2/\pi G\rho = 0.0901$ (for $q \ll 1$), shown here by the filled triangle. For values of angular velocity beyond the "Roche limit," no solution can be found for *any* combination of eccentricities.

3.2. Numerical Results

We have computed the equilibrium configurations of rotating binary systems for mass ratios, q, between 10^{-3} and 1. For each value of q, we found solutions starting at a very low angular velocity (large separation), for which the rotational and tidal deformations are small, and following a sequence of increasing angular velocity, ending at the Roche limit where an equilibrium solution can no longer be found.

In this section, we present examples of our numerical results for the equilibrium figures of rotation. These results were obtained using the numerical method described in Section 2, which allows the bodies to take *any* form that is symmetric about the $x-y$ and $x-z$ planes.[5] As we demonstrate below, in some cases our numerically computed equilibrium figures depart from an ellipsoidal form.

In Figure 3, we show several examples of equilibrium configurations. Panel (a) shows the equilibrium forms of equal-mass components, orbiting at a large separation (small angular velocity). The equilibrium figures in this case are, as expected, close to spherical. Panel (b) shows the same system orbiting at a closer separation (note different scale). Asphericity becomes apparent for this rapidly rotating system. The equilibrium configurations resemble triaxial ellipsoids, but departures from pure ellipsoidal forms can be readily seen.

Panel (c) shows an example of a smaller mass ratio, $q = 0.2$. In this case, the larger body is only mildly deformed due to the smaller gravitational perturbation of its low-mass companion. However, the smaller body is visibly distorted by the gravitational forces of its high-mass companion. Departures from ellipticity are apparent for the lower-mass component.

Finally, in panel (d) we show an extreme mass ratio, $q = 0.01$. For this system the center of mass is close to the center of the massive component. The lower mass satellite, is significantly deformed, yet remains nearly ellipsoidal (see Section 4.1). The

[5] The bodies are separated along the x axis, and the rotation is about the z axis.

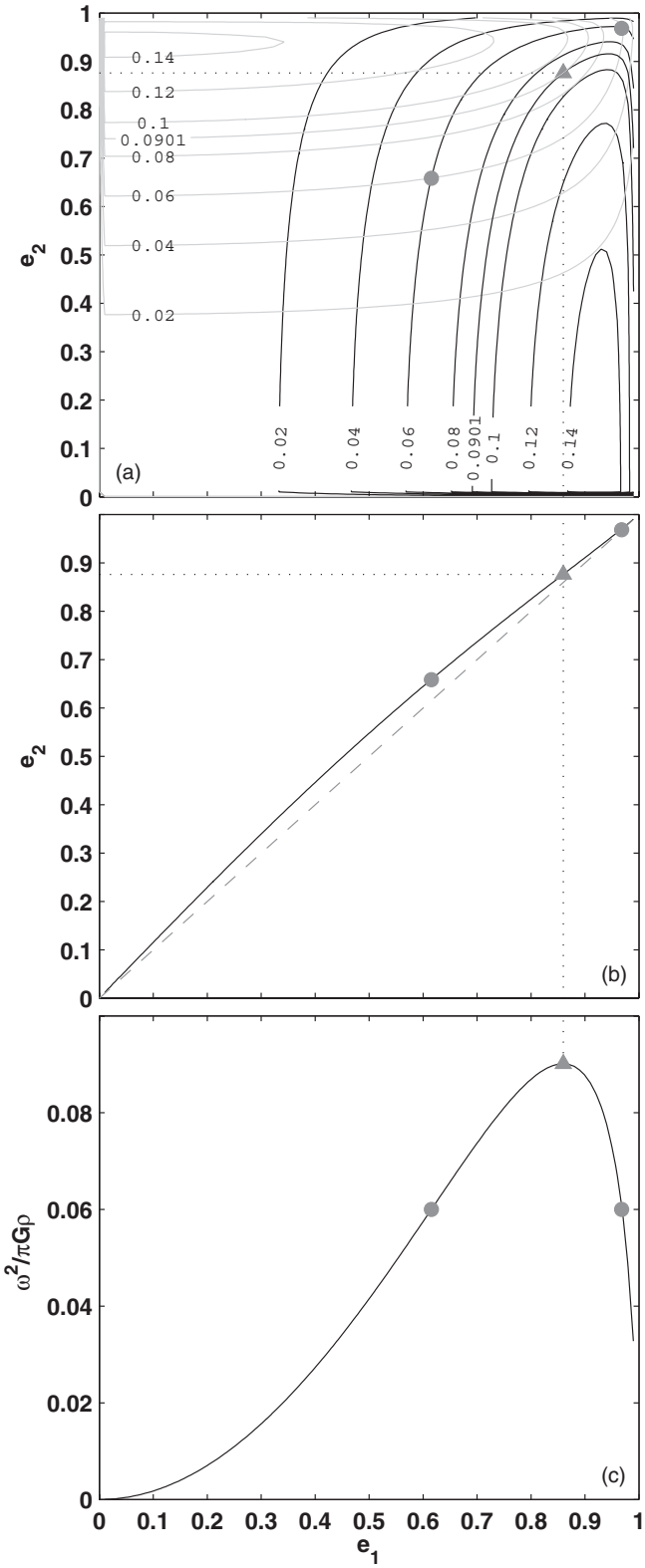

Figure 2. Roche Ellipsoid solutions for $q \ll 1$. Panel (a) shows the angular velocities given by Equations (14a) and (14b), (dark and gray contours) as functions of the eccentricities e_1 and e_2. A solution is found when dark and grey contours of equal values cross. For example, the filled circles show the two solution obtained for $\omega^2/\pi G\rho = 0.06$. The filled triangle is the single solution obtained for $\omega^2/\pi G\rho = 0.0901$. The solid curve in panel (b) shows the eccentricities of the Roche ellipsoid solutions. The solutions shown in panel (a) are displayed here again. Panel (c) shows the angular velocity associated with these solutions. The single solution for $\omega^2/\pi G\rho = 0.0901$ has the maximal possible angular velocity and is therefore the "Roche limit" ellipsoid.

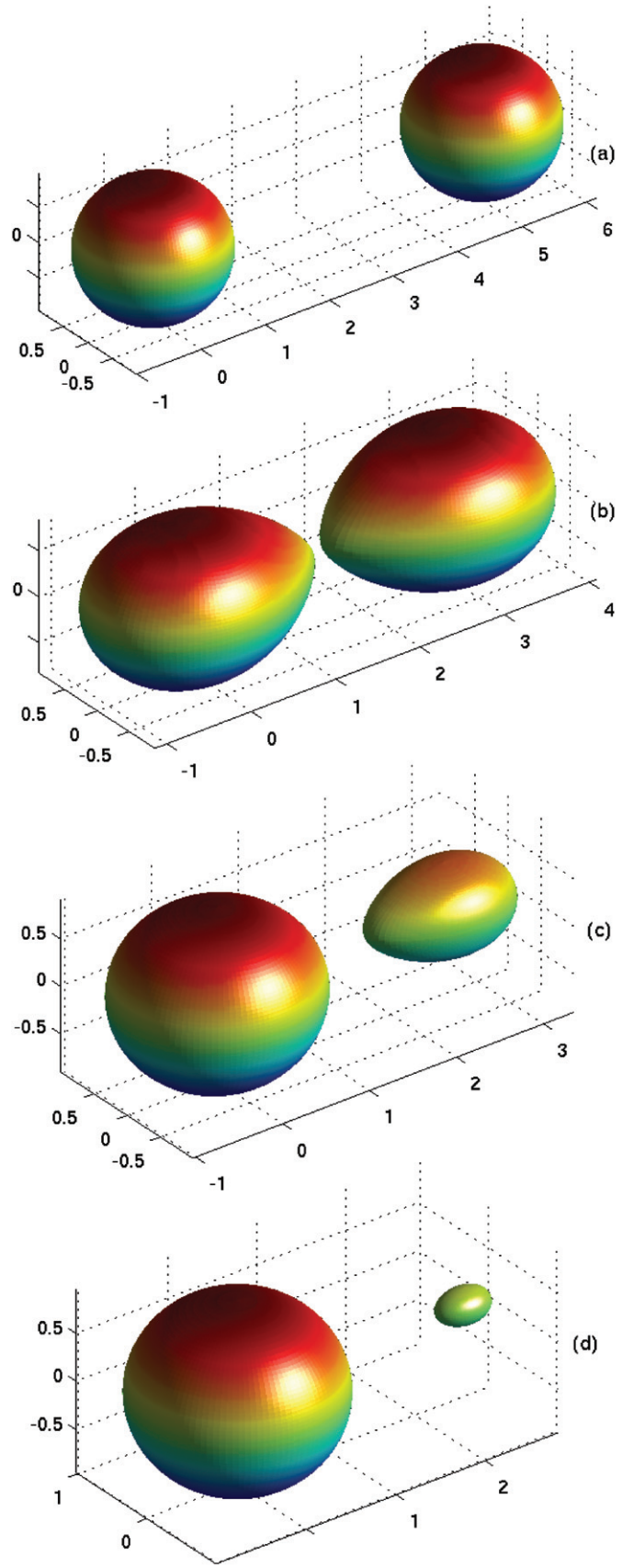

Figure 3. Equilibrium configurations of rotating binaries. (a) $q = 1$, distant components, (b) $q = 1$, close components, (c) $q = 0.2$, close components, (d) $q = 0.01$, close components.

(A color version of this figure is available in the online journal.)

massive component is unaffected by the minute gravity of its low-mass companion, and is deformed merely by its own rotation, thus taking the form of the oblate Maclaurin spheroid of the appropriate angular velocity.

4. DISCUSSION

4.1. Non-ellipticity

Consider the gravitational potential that a primary of mass M creates on the surface of its companion, which has a semimajor axis a, and is located at a distance d. On the axis connecting the two components,

$$V(a) = \frac{GM}{d}\left[1 - \frac{a}{d} + \left(\frac{a}{d}\right)^2 - \left(\frac{a}{d}\right)^3 + ...\right]. \quad (15)$$

The first term is constant, and does not produce any forces. The second terms gives rise to the circular orbital motion. The third term is the lowest order tidal force, which produces the symmetric deformations that were considered in the analysis of the Roche equilibrium ellipsoidal configurations (Section 3.1.3). The fourth term is the first *asymmetric* correction to the tidal potential, and is a factor a/d smaller than the previous term. Asymmetric deformation are therefore always small at large separations. In addition, the primary is not spherical, as it is also deformed by rotation and by tidal interactions. This affects the gravitational potential, and deviation from Equation (15) may also contribute to non-ellipsoidal deformations.

At a given separation, the semi-major axis of the lighter component is $\propto q^{1/3}$. For small values of q, the asymmetric correction to the potential is therefore small, and the bodies remain ellipsoidal to a good approximation (see Figure 3(d)). For larger values of q, the asymmetric corrections become significant.[6] Figure 4 shows an example of the departures from a symmetric ellipsoidal form, for $q = 0.3$, $d = 2.636$, and $\omega^2/G\rho = 0.29732$. The shaded area is the projection of our numerically computed equilibrium configurations on the x–z plane. The black contours show a projection of the best-fit ellipsoids. This example shows the asymmetric deformation of the lighter component. There is a significant "bump" on the side facing the primary, while the distant side is somewhat depressed. The primary's asymmetric deformation is minor.

To estimate the extent to which our equilibrium forms depart from pure ellipsoids, we fitted an ellipsoid to each numerically computed configuration, and then considered the differences between the best-fit ellipsoid surface and the numerical solution. In Figure 5, we display the departures from ellipsoidal configurations. The upper panels show the root mean square (rms) of differences between the two forms, $\sqrt{\sum(R_{i,\rm el} - R_{i,\rm sol})^2/N}$, where $R_{i,\rm el}$ is the distance from the center to the best-fit ellipsoid surface, $R_{i,\rm sol}$ is the distance from the center-of-mass to the surface of the numerical solution, and $i = 1, .., N$. The left-hand panel is for the primary, and the right hand panel is for the secondary. The rms of the primary (secondary) and the separation were normalized to the primary's (secondary's) mean radius. In each panel, different curves are shown for different values of q. The lowest curve is for the smallest mass ratio that we consider, 10^{-3}, followed by $q = 0.01, 0.1, 0.2, \ldots, 1.0$ in increasing order. Some labels are shown near the curves for guidance.

Figure 5 shows that ellipsoids are indeed a good fit at large separations, and become inaccurate at small separations. It also shows that for both of the components, the rms at a given distance increases as a function of q. At small separations and comparable mass ratios ($q > 0.2$) the typical rms is $\gtrsim 1\%$, and can be as large as $\sim 3\%$ for the most extreme cases.

The departures from ellipsoidal forms are most prominent in the direction facing the companion (see Figure 4). The rms may therefore remain relatively small even in cases where locally, large deviations occur. In the lower panels of Figure 5, we therefore show the largest deviation between the equilibrium configuration and its best ellipsoidal fit, for the primary (left panel) and secondary (right panel). At small separations and comparable mass ratios, a deviation of order 10% (20%) occurs for the primary (secondary) component.

4.2. Departures from Keplerian Rotation

The tidal and rotational deformations of the equilibrium configurations modify their gravitational potentials, causing them to deviate from those of spherical masses. These modified potentials affect the dynamics of the orbit, leading to departures from Keplerian rotation. For a given total mass and angular velocity, the separation is generally larger than that predicted by Kepler's law.

At large separations (small angular velocities), the bodies remain approximately spherical and the orbit is nearly Keplerian. At small separations (high ω), even for extreme mass ratios ($q \ll 1$), the rotational deformation of the primary leads to small departures from Keplerian rotation. For larger values of q, the effect grows, as triaxial and higher order deformations become significant.

Figure 6 shows the extent to which our numerical solutions depart from Keplerian rotation, measured in terms of $GM_{\rm tot}/\omega^2 d^3$. Keplerian rotation is given by the constant line $GM_{\rm tot}/\omega^2 d^3 = 1$ (dashed gray line). The numerical solutions for mass ratios between 10^{-3} and 1 are shown by the solid curves. Departures from Keplerian rotation are a growing function of the angular velocities for any q. For $q = 10^{-3}$, the maximal departure near the Roche limit is of order 1%. For comparable masses, departures of order 10% occur at the Roche limit, reaching a maximal value of $\sim 13\%$ for equal mass components.

4.3. Angular Momentum

In Figure 7 we show the angular velocity ($\omega^2/4\pi G\rho$) versus the angular momentum ($J/\sqrt{4\pi G}\rho^{3/2}V^{5/3}$, where V is the total volume). Different curves are for different mass ratios, between 10^{-3} (leftmost curve) and 1 (rightmost curve).

At a given mass ratio, the angular momentum first decreases as ω grows, but later begins to increase again. Each curve ends at a "Roche limit" appropriate for its mass ratio, where an equilibrium configuration can no longer be found.

Focus first on the data for $q = 10^{-3}$, shown again in Figure 8. For this extreme mass ratio, the system is rotating about the primary's center. Consider a primary of mass M and radius R, orbited by a satellite of mass $m = qM$ at a distance d. The angular momentum is the sum of two terms, an angular momentum due to primary spin,

$$J_{\rm spin} \simeq \frac{2}{5}MR^2\omega \quad (16)$$

[6] For eccentric orbits, the average gravitational potential deviates from a Keplerian potential, not only because of the deformations of the body inducing the potential, but also because of the changing distance along the eccentric orbit. If this distance change is much smaller than the deformations, the circular approximation holds (e.g., for the case of equal mass, near-contact binaries this implies $e < 0.01$). Our models do not apply to higher eccentricities.

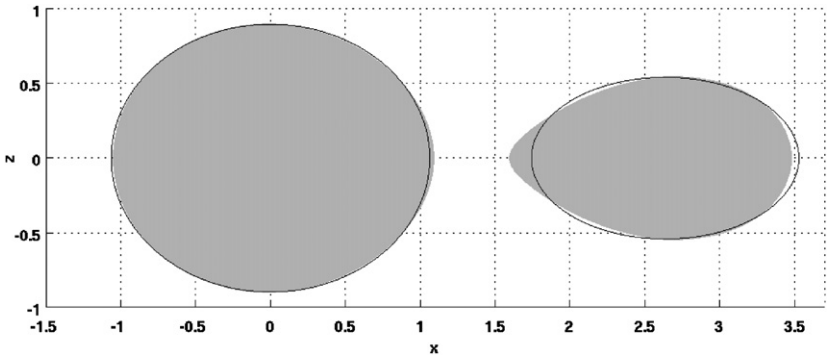

Figure 4. Departures from ellipsoidal form, for $q = 0.3$, $d = 2.636$, $\omega^2/G\rho = 0.29732$. The shaded area is the projection of the equilibrium configurations on the $x-z$ plane. The black contours show a projection of the best-fit ellipsoids.

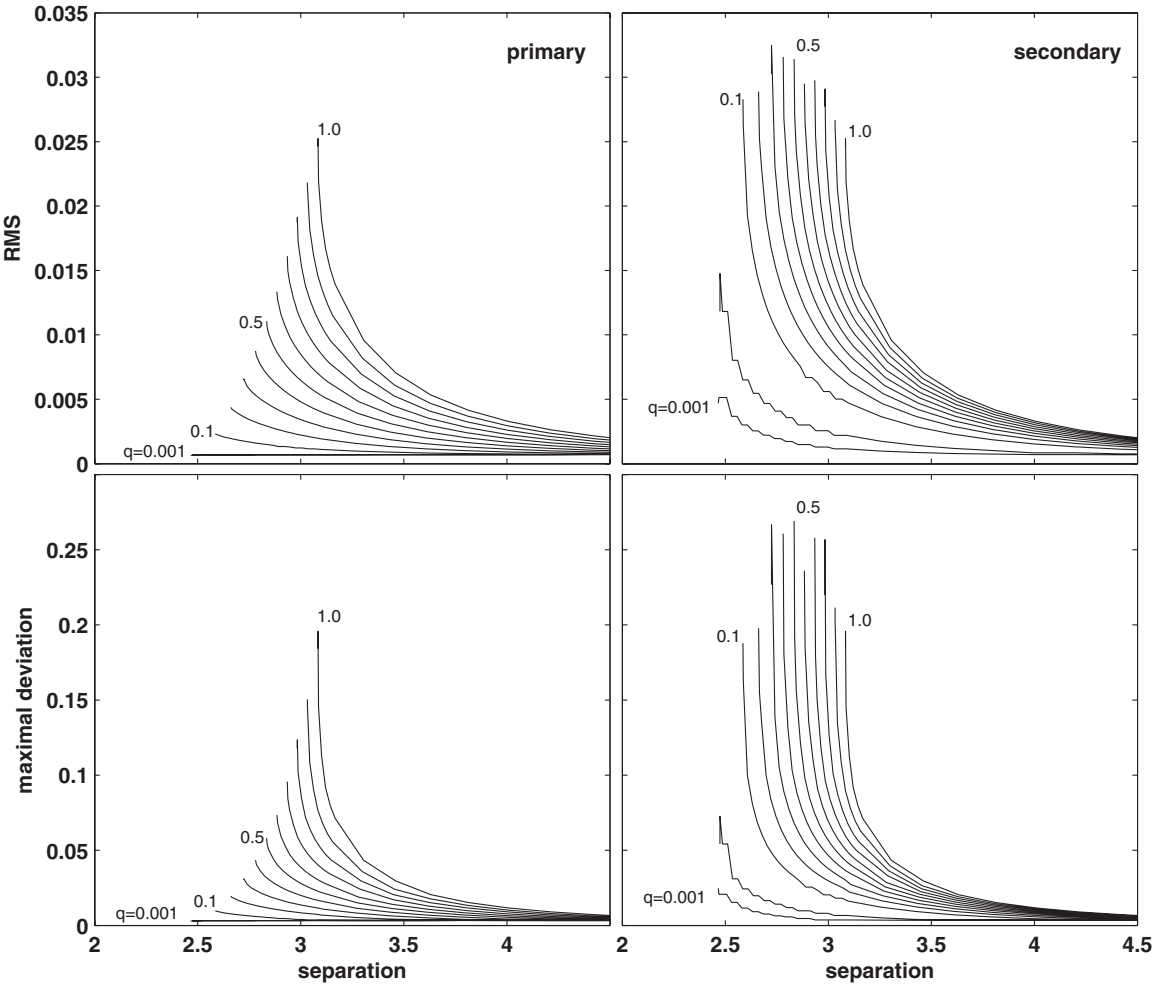

Figure 5. Departures from ellipsoidal configurations. The upper panels show the rms of differences in radii between our numerical configurations and triaxial ellipsoids fitted to them, as a function of separation. The lower panels show the maximal local deviation between the numerical results and the best-fit ellipsoids. The left hand panels are for the massive component (primary), and the right hand panels are for the secondary. Different curves are for different mass ratios, $q = 10^{-3},\ 10^{-2},\ 0.1,\ 0.2,\ 0.3, \ldots 1$. Some labels are indicated near the curves for guidance.

and an angular momentum due to the secondary orbit,

$$J_{\rm orbit} \simeq md^2\omega. \tag{17}$$

For Keplerian rotation, $J_{\rm orbit} \propto \omega^{-1/3}$.

At low angular velocities, the separation between the two components is large, and the orbital angular momentum dominates. As the angular velocity increases, $J_{\rm orbit}$ decreases, until the contribution of the primary's spin angular momentum begins to dominate, and the angular momentum is then proportional to ω.

This is shown in Figure 8. The dashed line shows the orbital angular momentum (Equation (17)) that dominates at small angular velocities. The dark solid curve is the primary spin angular momentum (Equation (16)) that dominates at large ω. The thick gray lines show the sum of both contributions. This simple analytic approximation nicely reproduces the trend followed by the numerical results.

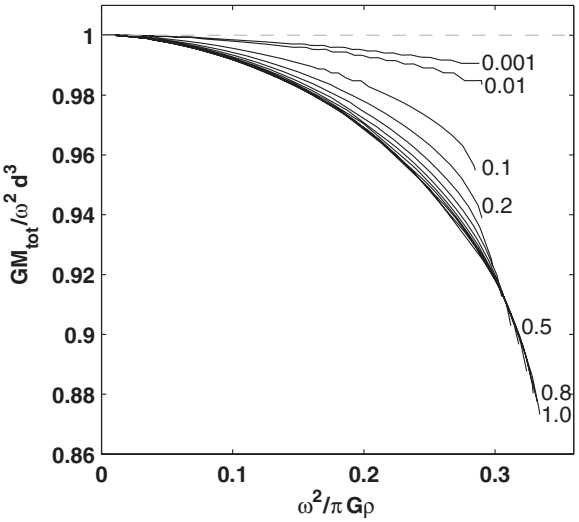

Figure 6. Departures (solid curves) from Keplerian rotation (dashed line) for mass ratios of 10^{-3}, 10^{-2}, 0.1, 0.2,... 1.0 (top to bottom). Some labels are indicated near the curves.

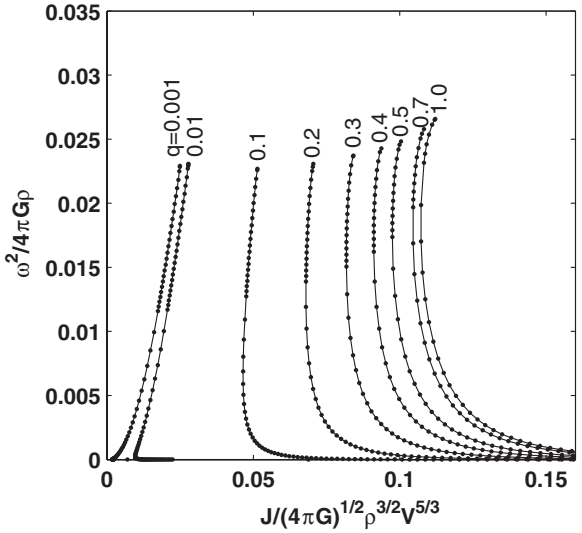

Figure 7. Angular velocity versus angular momentum for our numerical solutions. Data shown for q between 0.001 and 1, as indicated by the labels. Lines are shown to guide the eye in connecting points with the same q.

For less extreme mass ratios, the spin and orbit contributions due to both components must be taken into account. A simple analytical approximation may be derived under the simplifying assumptions of Keplerian rotation and a known deformation. Here we assume that the axes ratios for both components of the binary system, and for both axes in each component are equal, such that $b_1/a_1 = c_1/a_1 = b_2/a_2 = c_2/a_2 = \sqrt{1-e^2}$, where $a_i > b_i > c_i$ are the principle axes of the i'th components. In this approximation,

$$J_{\rm spin} = \frac{1}{5} M_1 a_1^2 (1+q^{5/3})(2-e^2)\omega \qquad (18)$$

and

$$J_{\rm orbit} = G^{2/3} M_1^{5/3} \frac{q}{(1+q)^{1/3}} \omega^{-1/3}. \qquad (19)$$

The total angular momentum is then given by

$$J = J_{\rm spin} + J_{\rm orbit}. \qquad (20)$$

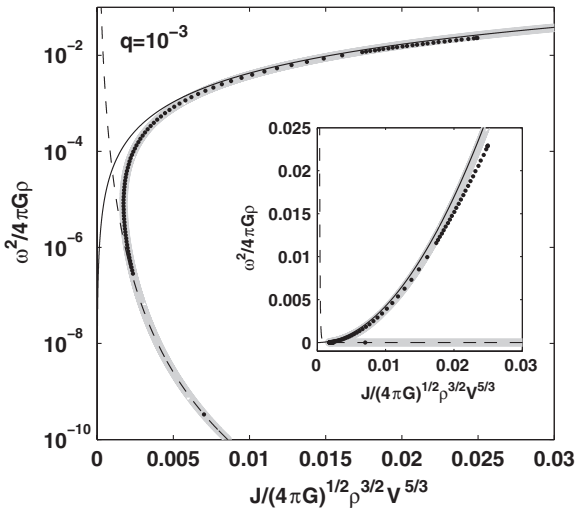

Figure 8. Angular velocity vs. angular momentum. The solid and dashed lines show the analytic expressions for the spin angular momentum of the primary, and orbit angular momentum of the secondary for $q \ll 1$. The thick gray line is the sum of both components. The points show the results of our numerical computations for $q = 0.001$. The inset shows the same data in linear scale.

At low angular velocities (large separations), the orbital angular momentum dominates, and J decreases with increasing ω. However, as the separation decreases, the contribution of the spin angular momentum increases, and J grows again.

For extreme mass ratios ($q \ll 1$), the larger component dominates the spin angular momentum, and the smaller component dominates the orbit angular momentum. The asphericity is limited to small (spheroidal) rotational deformations, and e remains close to 0. Equation (20) thus agrees with its simplified version above (Equations (16) and (17)). As the value of q grows, the tidal forces deform the bodies, and the configurations grow increasingly aspherical.

In Figure 9, we focus on the angular momentum for $q = 1$. The data points show our numerical solutions, and the different curves show the analytical approximations of Equation (20) for $q = 1$ and for increasing values of eccentricity. The leftmost solid curve is for spheres ($e = 0$), and curves to the right are for higher eccentricities. At small angular velocities (large separations), the tidal and rotational deformations remain minor, and the spherical approximation agrees with the numerical results. As ω increases, tidal forces deform the bodies into increasingly elongated shapes. Figure 9 indeed shows that as ω increases, the values of J grow further and further away from the spherical $e = 0$ curve. In fact, as ω increases the values of J continuously shifts to curves of higher and higher eccentricity.

We return now to Figure 7. The angular velocity at which the angular momentum achieves its minimum is an increasing function of q. According to Equation (20), this occurs at $\omega^2 \propto q^{3/2}(1+q)^{-2}(1+q^{5/3})^{-3/2}$. The angular momentum of equal mass binaries therefore "turns around" at a higher value of ω than for binaries with extreme mass ratios.

The approximation of Equation (20) thus explains the existence of a minimum to the angular momentum, the position of this minimum as a function of q, and the "drift" of the angular momentum to values larger than those expected for spheres.

5. LIGHT CURVES

We have carried out computations of the light curves of Kuiper Belt binaries based on the equilibrium figures of rotation

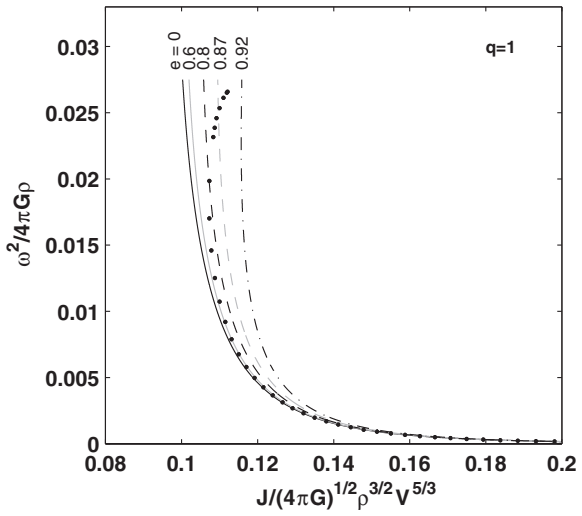

Figure 9. Angular velocity versus angular momentum for $q = 1.0$. The points show our numerical results. The different curves show the analytic approximation of Equation (20) for various values of eccentricity ($e = 0, 0.6, 0.8, 0.87, 0.92$), as indicated by the labels. As ω increases, tidal deformations grow, and the value of J continuously shifts to curves of higher eccentricity.

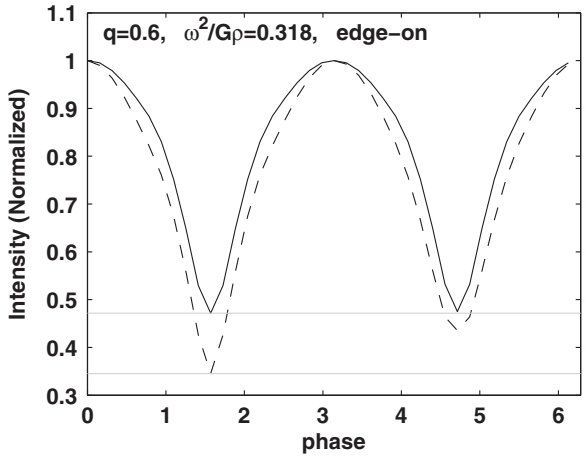

Figure 10. Light curves of an edge-on binary system with $q = 0.6$ and $\omega^2/G\rho = 0.318$. The solid curve is for backscatter reflection, and the dashed curve is for diffuse reflection.

presented in Section 3.2. The light curves depend on the relative positions of the observed binary, the observer, and the light source; on the inclination of the orbit relative to the plane of the sky; and on the reflecting properties of the materials composing the surface of the observed system.

For binaries in the Kuiper Belt the observed geometry is simple. At a distance of $\gtrsim$40 AU, the observer (on Earth), light source (the Sun), and the observed Kuiper Belt binary are almost aligned, so that the "phase angle" between the line of sight and the KBO–Sun direction always remains small ($<2^\circ$).

The reflecting properties of KBOs are not well constrained. Here we consider two simple options. First, we consider uniform reflection, which produces an observed intensity proportional to the projected area on the plane of the sky. For the given geometry, this can result from simple "backscatter" reflection.[7] Second, we study the case of diffuse ("Lambertian") reflection, for which light is reflected equally in all directions, and the observed intensity from a surface area depends only on the cosine of the angle between the Sun and the normal to the reflecting surface.

The absolute intensity of light as seen from Earth also depends on the distances between the Sun, the KBO, and Earth, and on the KBO's size and albedo. Here we ignore the absolute intensities and instead focus on the normalized relative light curves. We tile the surface of a given equilibrium configuration with surface triangles, and then compute the light intensity for a given orbital phase, inclination, and reflection law, taking into account possible obscurations of different tiles. The numerical procedure is described in detail in Appendix B. We have verified that our results reproduce previous light-curve computations given similar configurations (see Appendix B.2).

In Figure 10, we show an example of a light curve computed for a mass ratio $q = 0.6$, an angular velocity $\omega^2/G\rho = 0.318$, and an edge-on orbit. The solid curve shows the light curve for backscatter reflection, and the dashed curve is for diffuse (Lambertian) reflection. Both light curves have been normalized so that the intensity equals 1 at the maximum (note that for a given albedo the absolute intensity is larger for backscatter reflection).

The light curve shape depends on the orbital parameters. In large separation (small ω) binaries, the eclipses only span a small fraction of the orbit, and the light curves generally appear to be slowly varying outside of the eclipses, as the projected area gradually changes. In close binaries (large ω), such "plateaus" do not exist between the two eclipses. For the mass ratio considered in Figure 10, $\omega^2/G\rho = 0.318$ corresponds to a close binary, and the eclipses indeed appear to span most of the orbit.

The mass ratio determines the depth of the eclipses. Even for the case of backscatter reflection, for which the intensity is proportional to the projected area, eclipses are deepest for equal mass components. In this case, the tidal deformations are largest, and the projected area is a strong function of orbital phase. The deformations for extreme-mass ratio binaries are smaller (and more spheroidal), and the relative depth of the eclipses is thus smaller. For diffuse reflection, the impact of the mass ratio is even larger. One of the most indicative differences between backscatter and diffuse reflections is the relative depth of the two minima. In backscatter reflection, which is sensitive only to the total projected area, the depths of the two minima are always equal, regardless of whether the small body is in front of the large body or vice versa. However, for diffuse reflection, which is sensitive to the surface curvature, the two minima exhibit different depths. When the small body is viewed in front of the large body, a larger fraction of the surface is inclined relative to the light source, and so the reflected intensity is smaller. An additional parameter that affects the depth of the eclipses is the orbital inclination. Figure 10 shows the maximal variation that obtains for an edge-on orbit. Higher inclinations result in smaller variations.

Next we examine the differences between light curves computed assuming the Roche approximation and light curves computed using our numerical solution. As an example, we consider the light curve of an equal mass binary, with an angular velocity $\omega^2/G\rho = 0.316$. In Figure 11, we show the ratio between the light intensity resulting from the Roche configuration appropriate to this angular velocity, and our non-ellipsoidal non-Keplerian configurations. Both light curves were computed using the numerical procedure described in Appendix B, assuming

[7] The Lommel–Seeliger law also reduces to being proportional to the geometrical cross-section at low phase angles (e.g., Lacerda & Jewitt 2007).

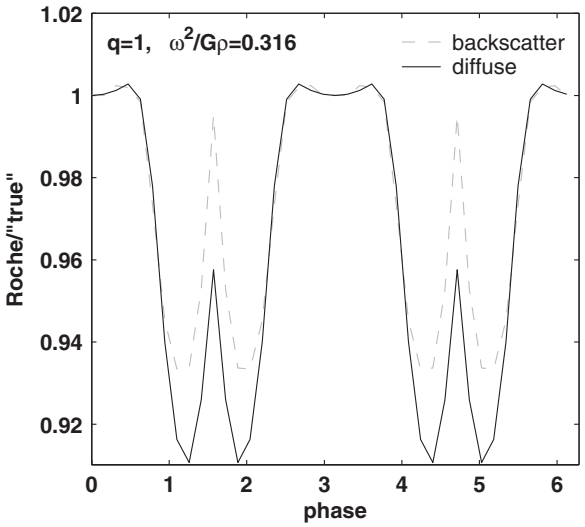

Figure 11. Ratio between the Roche-approximation and numerically computed-configurations light intensities as a function of orbital phase, for an equal mass binary with $\omega^2/G\rho = 0.316$. In both cases we assumed an edge-on orbit. The solid curve is for diffuse reflection, and the dashed curve is for backscatter. The maxima of the individual light-curves occur at a phase of 0 and π.

edge-on inclination. They differ only by the equilibrium forms. The phase is defined so that the maxima of each individual light curve is obtained at 0 and π.

Figure 11 shows that light curves differ by up to ∼10%, and that the ratio between the two cases is a function of orbital phase. Intensity variations of ∼10% can be easily detected with current facilities, and the numerical configurations may thus produce superior fits to observed data, and provide better constrains on the physical parameters of the observed system.

6. APPLICATION TO KUIPER BELT BINARY 2001 QG_{298}

6.1. Observational Review

2001 QG_{298} has been discovered as part of the Hawaii Kuiper Belt Variability Project (Jewitt & Sheppard 2002; Sheppard & Jewitt 2002, 2003). The observations, carried out with the University of Hawaii's 2.2 m telescope and with the Keck 10 m telescope, are reported in Sheppard & Jewitt (2004, hereafter SJ04). SJ04 indicate that 2001 QG_{298} has a peak-to-peak photometric range of 1.14 ± 0.01 mag in the *R* band, and a period of 6.8872 ± 0.0002 hr for a single-maximum period (which may arise due to albedo variations), or 13.7744 ± 0.0004 hr for a double-maximum period (which may arise due to rotation). SJ04 note that the double-peaked light curve provides a better fit to the observed data, for which the two minima differ by about 0.1 mag. Furthermore, Keck *VBR* colors of 2001 QG_{298} indicate no color variations along the period, within the photometric uncertainties of a few percent.

The observed amplitude variation of 1.14 mag is exceptionally large among large (>25 km) solar system objects. SJ04 discuss three possible reasons for the large photometric range. First, they consider the possibility of albedo variations, and conclude that this scenario is unlikely. On asteroids, albedo brightness variations are usually smaller than 10%–20%. Larger albedo variations are likely to be associated with color variations (e.g., Iapetus). Finally, the fact that a double-peaked period provides a better fit with two distinct minima favors a light curve produced by rotation rather than by albedo variations.

Next, they consider the possibility of an elongated shape. SJ04 use the observed photometric range to infer an axis ratio $b/a = 0.35$ (assuming the intensity is proportional to the projected area). Given the absolute luminosity of 2001 QG_{298}, they derive a semi-major axis between 170 and 270 km for "typical" KBO albedos range (0.04–0.1). Bodies of this size are unlikely to be held by material strength over long timescales. Gravity-dominated bodies are rotationally deformed into Maclaurin spheroids or Jacobi ellipsoids, depending on their angular velocity. SJ04 note that the maximal photometric range for stable Jacobi ellipsoids is 0.9 mag, lower than the observed variation of 2001 QG_{298}. This maximum variation occurs for a Jacobi ellipsoid with $b/a = 0.432$ and $c/a = 0.345$ (Chandrasekhar 1969; Farinella et al. 1981) and more elongated objects are dynamically unstable. However, we note here that the maximum variation quoted in SJ04 applies to backscatter reflection, whereas for diffuse (Lambert) reflection these axis ratios yield a variation of 1.5 mag. SJ04 also note that the rotational period of 2001 QG_{298} is too long to cause significant elongation for reasonable densities. They conclude that 2001 QG_{298} is unlikely to be a single rotating object.

Finally, SJ04 consider the possibility of a close binary configuration. As discussed above, the components are distorted both by rotation and tidal forces. The photometric range of 2001 QG_{298} is consistent with that of a comparable mass close binary Roche configuration (Leone et al. 1984). They conclude that given the large amplitude variation, long period, and difference between the two minima, a close binary is the most likely explanation for 2001 QG_{298}.

With the binary scenario, several attempts have been made to derive the physical properties of 2001 QG_{298} using the Roche ellipsoidal approximations. SJ04 used the results presented in Leone et al. (1984) to estimate the density, and find $\rho \sim 1$ g cm^{-3}. Takahashi & Ip (2004) then constructed specific Roche binary light curve simulations to fit the observed light curve. Their best fit Roche solution implies that 2001 QG_{298} consists of two components with a mass ratio of 0.65. Their primary has axis-ratios $b/a = 0.79$ and $c/a = 0.62$, and their secondary has $b/a = 0.61$ and $c/a = 0.56$. The separation is 2.1 times the primary's semi-major axis (see the illustration in Appendix B.2). This solution indicates a "mixed" reflection pattern, with ∼70% diffuse reflection and ∼30% backscatter (uniform) reflection. For these parameters, they infer a bulk density of 0.63 ± 0.20 g cm^{-3}.

Later, Lacerda & Jewitt (2007) presented an additional model for 2001 QG_{298}. In their solution, the mass ratio is 0.84. Their primary has $b/a = 0.62$ and $c/a = 0.65$, and their secondary $b/a = 0.45$ and $c/a = 0.41$. The separation is 2.1 times the primary semi-major axis (see the illustration in Appendix B.2). Lacerda & Jewitt find that backscatter reflection best fits the observed data, and they infer a bulk density of $0.590^{+0.143}_{-0.47}$ g cm^{-3}. Lacerda & Jewitt also considered the possibility that 2001 QG_{298} is in fact a single Jacobi ellipsoid with diffuse (Lambert) or backscatter reflection. They conclude that the Roche models fit the data significantly better than Jacobi ellipsoids.

In the next section, we apply our numerical models to 2001 QG_{298}, and demonstrate how our more accurate solutions can be used to constrain the physical properties of KBO binaries.

6.2. Light Curve Fitting and Analysis

We are interested in finding a physical configuration consistent with the observations of 2001 QG_{298}. To this end, we compare the light curves associated with the equilibrium

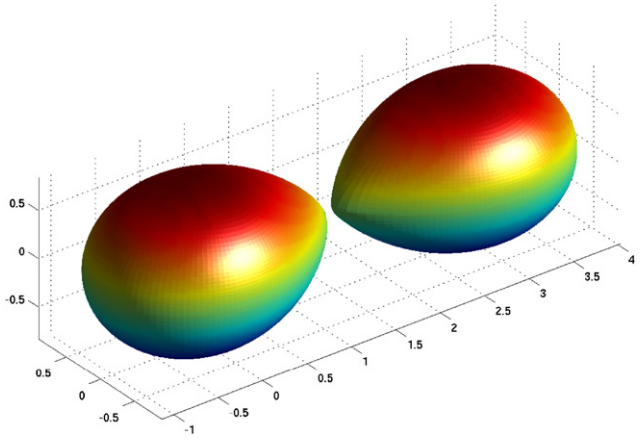

Figure 12. Best-fit configuration for 2001 QG_{298}.
(A color version of this figure is available in the online journal.)

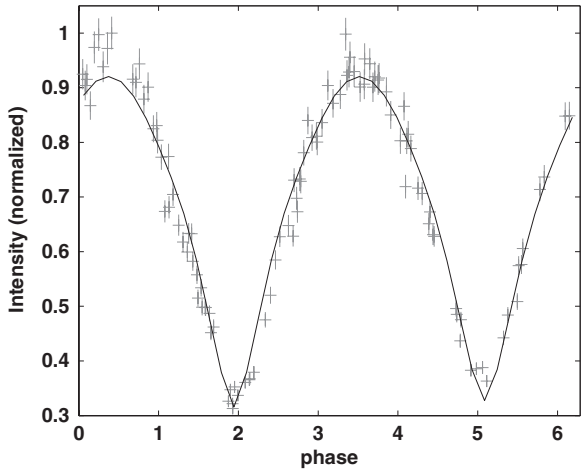

Figure 13. Observed light curve for QG_{298} (data points) and best-fit solution (solid curve), obtained for $q = 0.93$, $\Omega^2/G\rho = 0.333$, with Lambertian reflection at an inclination of 3°.

configurations computed in Section 3 with the observed light curve of 2001 QG_{298} (SJ04), after correcting for the light travel-time and phase angle effects.

To find the best fit, we create a library of light curves for comparison with observations. However, because the light curve calculations are computationally expensive, we approached the fitting procedure in two steps. First, we created a library of "low-resolution configurations." Here we used equilibrium configurations computed with 200 patches on a quarter-sphere, to construct light curves spanning the entire parameter space studied in Section 3. Given this library of light curves, we found the best fit (in the sense of minimum χ^2) model.

For each model, which corresponds to a specific combination of mass ratio, rotational velocity, and inclination, we fitted two parameters: α and β. These are the overall normalization factors for a "mixed" light curve composed of both backscatter and diffuse reflection, such that the total intensity is $I = \alpha\, I^{\rm Backscatter}_{\rm model} + \beta\, I^{\rm Diffuse}_{\rm model}$. In addition to these two normalization parameters, we allowed for a relative constant phase-shift between the observed and computed light curves.

Given the best fit solution for the "low-resolution configurations" library, we computed a better-sampled, dense library of light curves based on "high-resolution configurations," which have 1600 patches on a quarter sphere. For the high resolution configurations, we focus on the parameter-space surrounding the "low-resolution" solution. We again searched for the best-fit solution among this new set of model light curves.

The best-fit solution is illustrated in Figure 12. This model has a mass ratio $q = 0.93$ and a rotational velocity $\Omega^2/G\rho = 0.333$. The best fit is found for pure diffuse (Lambertian) reflection (so that $\alpha = 0$), viewed at an inclination of 3°. For the observed period of 2001 QG_{298}, these parameters imply a density $\rho = 0.72$ g cm^{-3}. The observed magnitude then implies masses of $1.70 \times 10^{18}(A/0.1)^{-1.5}$ and $1.58 \times 10^{18}(A/0.1)^{-1.5}$ kg for the two components, where A is the albedo. While our bodies are not ellipsoidal, an ellipsoidal fit yields semimajor axes of $102 \times 78 \times 71$ and $102 \times 75 \times 69$ km^3.

We display the observed light curve (symbols) along with the best fit model (solid curve) in Figure 13. For our assumed intensity errors of 3.5% on the computed light curves and 4% on the observed data, this models yields a χ^2 of 123.4 for 107 degrees of freedom.[8]

[8] For 112 observed data points and five fitted parameters, namely the mass ratio, angular velocity, inclination, values of α and β, and the global phase shift.

To estimate the errors on the best fit parameters, we inspect the values of χ^2 obtained for other models. With five fitted parameters and a minimal χ^2 of 123.4, models with $\chi^2 < 129.3$ are within the 1σ (68.27%) error region. Inspecting the model library, we derive the following 1σ error regions: for the mass ratio, $0.9 < q < 1.0$; for the angular velocity, $0.332 < \omega^2/G\rho < 0.334$; and for the inclination, $2° < i < 4°$. We further find that all acceptable models have "pure" diffuse reflection. Given the observed period (and error), the error on the angular velocity can be used to compute the error on the bulk density. We find a 5.6% error on the density, $\rho = 0.72 \pm 0.04$ g cm^{-3}.

7. SUMMARY

In this paper, we introduce a numerical method for computing the self-consistent equilibrium configurations of tidally-locked homogeneous binaries, rotating in circular orbits. The equilibrium configurations depend on the mass ratio, angular velocity, and separation between the two components.

We explicitly compute the gravitational and rotational potentials on the surface of the two components, and use a Newton–Raphson-based scheme to converge to an equilibrium solution, for which the surfaces of each of the bodies is an equipotential surface. Our numerical procedure is described in detail in Section 2 and Appendix A.

In Section 3, we discuss the properties of the equilibrium figures of rotation. We begin with simple analytic approximations that we use to study the characteristics of the equilibrium solutions. We confirm that for low angular velocities (large separations), two equilibrium configurations always exist, differing by their eccentricity. The low eccentricity solution is stable. A flattening of the low-eccentricity configuration results in restoring forces. The high-eccentricity solution is unstable. A flattening of the equilibrium configuration results in forces that act to flatten it even further, driving the eccentricities away from the equilibrium values.

As the angular velocity increases, there exists a "limiting" angular velocity for which only one equilibrium solution exists. This is known as the "Roche limit" configuration. For even higher angular velocities, no equilibrium solution can be found. At the Roche limit, the material is still bound, and so the Roche limit is crossed before the Roche lobe is filled. However, once

the Roche limit is crossed, the configuration is driven to an ever increasing eccentricity, and eventually mass shedding will occur as material flows beyond the Roche-lobe.

We find numerical solutions for the equilibrium configurations for mass ratios, q, between 10^{-3} and 1. For each value of q we find solutions starting at a very low angular velocity (large separation), for which the rotational and tidal deformations are small, and following a sequence of increasing angular velocity, terminating at the Roche limit where an equilibrium configuration can no longer be found.

Our numerical solutions indicate that the equilibrium configurations are not always ellipsoidal. Ellipsoidal fits are generally good approximations at large separations and for extreme mass ratios. Even at small separations and for comparable masses, the typical rms deviation between a numerical solution and an ellipsoid fitted to it is 1%–3%. However, departures from ellipsoidal forms are most pronounced in the direction facing the companion, and the maximal local deviations from ellipsoidal forms are of order 10% (20%) for the primary (secondary) component.

The tidal and rotational deformations of the equilibrium configurations modify their gravitational potentials. This, in turn, affects the dynamics of the orbit, leading to departures from Keplerian rotation. We measure departures from Keplerian rotation in terms of $GM_{\rm tot}/\omega^2 d^3$. At large separations the bodies remain approximately spherical, departures from Keplerian rotation remain small, and $GM_{\rm tot}/\omega^2 d^3 \sim 1$ as it should be. At small separations, departures from Keplerian rotation appear. For $q = 10^{-3}$ the maximal deviation near the Roche limit is $\sim$1%. For comparable masses ($q > 0.5$), deviations of order 10% occur at the Roche limit, reaching a maximal value of $\sim$13% for equal mass components.

We inspect the angular momenta of the equilibrium configurations. We decompose the angular momenta into "spin" and "orbit" components, and explain the trends in the angular momentum-angular velocity parameter-space. As the angular velocity increases, it shifts from being orbit-dominated to being spin-dominated, creating a minimum in the angular momentum. We discuss the increasing value of this minimum with increasing mass ratio, and demonstrate the "drift" of the angular momentum to higher values as the tidal deformations grow.

In Section 5, we calculate the light curves that arise from our numerically computed equilibrium configurations, if placed in the Kuiper Belt. In addition to the configurations, the observed light curves also depend on the inclination of the orbit relative to the plane of the sky, and on the reflecting properties of the surface of the objects.

We consider two possibilities for the reflecting properties. First we consider an observed intensity that is proportional to the projected area on the plane of the sky, as is appropriate for backscatter reflection from Kuiper Belt objects. Second, we consider the possibility of diffuse (Lambert) reflection in which the reflected light from a surface area is proportional to the cosine of the angle between the sun and the normal to the surface. We note that backscatter reflection is sensitive only to the total projected area, and therefore always yields two equal minima. However, diffuse reflection, which is sensitive to the surface curvature, generally produces two minima of different depths. When the small body is viewed "in front" of the large body, a larger fraction of the surface is inclined.

We compare our light curves to those resulting from the classical Roche ellipsoidal approximations, and find phase-dependent intensity deviations of $\lesssim$10% between the two cases.

Finally, in Section 6 we apply our numerical models to Kuiper Belt binary 2001 QG_{298}. This object exhibits an extremely large photometric range of 1.14 ± 0.01 mag (R-band), and a double-peaked period of 13.7744 ± 0.0004 hr. It is believed to be an example of a close-binary Kuiper Belt population (SJ04).

Our numerical models indicate that 2001 QG_{298} is well fitted by a binary with a mass ratio $q = 0.93^{+0.07}_{-0.03}$, an angular velocity $\omega^2/G\rho = 0.333 \pm 0.001$, a nearly edge-on inclination, $i = 3 \pm 1^\circ$, and pure diffuse reflection. For the observed period of 2001 QG_{298}, these parameters imply a bulk density, $\rho = 0.72 \pm 0.04$ g cm^{-3}.

SJ04 estimate that 2001 QG_{298} is a representative of a large Kuiper Belt population of nearly-contact binaries, and that at least 10%–20% of all large KBOs are, in fact, close-binaries. Upcoming LSST observations will identify >20,000 new KBOs (LSST Science Collaborations: Abell et al. 2009). If indeed a significant fraction of the large KBO population is in the form of contact binaries, the models and methods outlined in this paper may become essential for the interpretation of their light curves.

We thank Oded Aharonson, Peter Goldreich, Ehud Nakar, Eran Ofek, David Polishook, and Hilke Schlichting for helpful discussions. Some of the numerical calculations presented in this work were performed on Caltech's Division of Geological and Planetary Sciences Dell cluster. We thank Oded Aharonson for his assistance with our use of the cluster. O.G. acknowledges support provided by NASA through Chandra Postdoctoral Fellowship grant number PF8-90053 awarded by the Chandra X-ray Center, which is operated by the Smithsonian Astrophysical Observatory for NASA under contract NAS8-03060. The research of R.S. is supported by IRG and ERC grants, and a Packard Fellowship.

APPENDIX A

BASIC EQUATIONS AND NUMERICAL PROCEDURE

A.1. Definitions

We are interested in finding self consistent equilibrium configurations of a tidally locked binary systems, comprised of two homogeneous components, rotating in a circular orbits.

The parameters governing the equilibrium configurations are the mass ratio $q \equiv M_2/M_1 < 1$; the scaled angular velocity $\omega^2/G\rho$; and the separation between the components' center of masses, d. In Keplerian rotation, the angular velocity, separation, and total mass are related via Equation (6). However, here we allow departures from Keplerian rotation. When searching for equilibrium configurations, we treat the separation and angular velocity as two independent parameters, and solve for the total mass of the system.

We first define a Cartesian coordinate system, whose origin is at the center of the more massive component, M_1. We define the $\hat{x}$ direction to point toward the lighter companion, M_2, which is centered at $x = d$. The common center of mass is located at $x = qd/(q+1)$. We define the $\hat{z}$ direction to be parallel to the angular velocity. Figure 14 illustrates the choice of coordinates.

We describe the surface of each body relative to its *own* center of mass using a spherical coordinate system. The surface of each component is sampled along N points with given angular directions, specified by the azimuthal angle ϕ and the polar angle

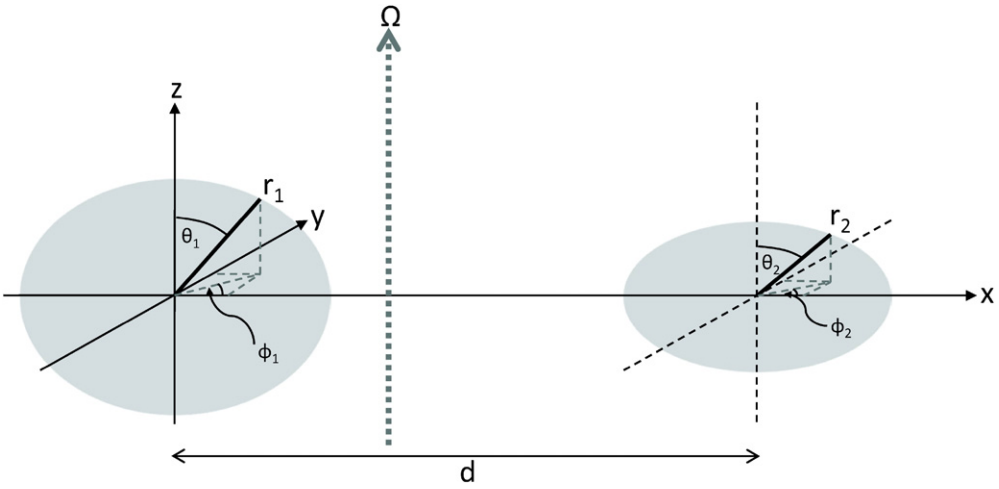

Figure 14. A schematic representation of the coordinates used in the numerical solution.

θ defined in the usual way. For example, in Figure 14,

$$\begin{cases} x_1 = r_1 \sin(\theta_1)\cos(\phi_1) \\ y_1 = r_1 \sin(\theta_1)\sin(\phi_1) \\ z_1 = r_1 \cos(\theta_1) \end{cases} \quad \begin{cases} x_2 = d + r_2 \sin(\theta_2)\cos(\phi_2) \\ y_2 = r_2 \sin(\theta_2)\sin(\phi_2) \\ z_2 = r_2 \cos(\theta_2) \end{cases} . \tag{A1}$$

The surface mapping is performed by associating each direction (ϕ_i, θ_i) with the distance, along this direction, between the center of mass and the surface, R_i.

Each of the N points correspond to a small surface area surrounding it. We distribute the N points evenly in ϕ and in $\cos(\theta)$ to ensure that each point covers an equal solid angle $\Delta\Omega$, as measured from the center of the body. We assume that the equilibrium configurations are symmetric about the $x-y$ and $x-z$ planes. This assumption allows us to only sample a quarter of a sphere when mapping the surface of each body.

Each surface patch corresponds to a "mass cone" stretching from the patch to the center of the body. For homogeneous bodies, the mass within the i'th "cone," stretching from $r = 0$ to the surface where $r = R_i$, is $M_i = \int_0^{R_i} \rho r^2 \Delta\Omega dr = \Delta\Omega\rho R_i^3/3$. The total mass in the body is $M = \sum_i M_i = \Delta\Omega\rho/3 \times \sum_i R_i^3$.

The potential at a point located on the surface of a body is the sum of the gravitational potentials induced by the mass in all the cones in both components, and the rotational potential about the common center of mass. Our goal is to solve for the values of R_i, for which the total potential along the surface of each body is constant. While the surface of each body must be equipotential, the values of the potential may differ between the two bodies.

A.2. Evaluating the Potential

To compute the gravitational potential at some surface point, we must first evaluate the distance between this point and a mass element dm inducing the potential. We can write the distance between two points that belong to M_1 or M_2, (ϕ_i, θ_i, r_i) and (ϕ_j, θ_j, r_j) as

$$\Delta r^2 = r_i^2 + A r_i + B \tag{A2}$$

with

$$A = a r_j \pm 2l \sin(\theta_i)\cos(\phi_i), \tag{A3a}$$

$$B = l^2 + r_j^2 \mp 2 l r_j \sin(\theta_j)\cos(\phi_j) \tag{A3b}$$

where

$$a = -2\{\sin(\theta_i)\sin(\theta_j)[\cos(\phi_i)\cos(\phi_j) + \sin(\phi_i)\sin(\phi_j)] + \cos(\theta_i)\cos(\theta_j)\} \tag{A4}$$

and

$$l = \begin{cases} d, & i, j \text{ in different components} \\ 0, & i, j \text{ in same component} \end{cases} . \tag{A5}$$

the plus [minus] sign in Equations (A3a) [(A3b)] should be used if j is in M_1 and i is in M_2, and the minus [plus] sign should be used if j is in M_2 and i in M_1. If both points are in the same mass, $l = 0$ such that $A = a r_j$ and $B = 0$.

Given this distance, the gravitational potential due to the total mass in cone i with extent R_i, at a point (ϕ_j, θ_j, r_j) is

$$\begin{aligned} V_i(r_j) = \Delta\Omega_i \Bigg\{ & \left(\frac{R_i}{2} - \frac{3A}{4}\right)\sqrt{R_i^2 + A R_i + B} + \frac{3A}{4}\sqrt{B} \\ & + \left(\frac{3A^2}{8} - \frac{B}{2}\right)\ln\left(\frac{A}{2} + R_i + \sqrt{R_i^2 + A R_i + B}\right) \\ & - \left(\frac{3A^2}{8} - \frac{B}{2}\right)\ln\left(\frac{A}{2} + \sqrt{B}\right)\Bigg\}, \end{aligned} \tag{A6}$$

where A and B are the functions of r_j specified by Equation (A3), and $\Delta\Omega_i$ is the solid angle covered by cone i.

For the rotational potential at a point (ϕ_j, θ_j, r_j) we can write

$$V_{\rm rot} = \frac{1}{2}\omega^2 \begin{cases} \left(\frac{qd}{q+1}\right)^2 + r_j^2 \sin(\theta_j)^2 \\ \qquad -\frac{2qd}{q+1} r_j \sin(\theta_j)\cos(\phi_j), & j \text{ in } M_1 \\ \left(\frac{d}{q+1}\right)^2 + r_j^2 \sin(\theta_j)^2 \\ \qquad +\frac{2d}{q+1} r_j \sin(\theta_j)\cos(\phi_j), & j \text{ in } M_2 \end{cases} . \tag{A7}$$

A.3. The Newton–Raphson Scheme

Consider a model with N_1 points sampling the surface of M_1, and N_2 points sampling the surface of M_2. The conditions of constant-potentials provides $N_1 + N_2$ equation. For points R_j on the surface of M_k these equations can be written as

$$\sum_{i \in M_1} V_i(R_j) + \sum_{i \in M_2} V_i(R_j) + V_{\rm rot}(R_j) - c_k = 0 . \tag{A8}$$

The variables in these equations are the $N_1 + N_2$ values R_i, and the values of the constant potentials on the surfaces of the two components, c_1 on M_1, and c_2 on M_2.

Two additional equations are therefore required to solve the problem. One of these equations is the constraint provided by the given mass ratio, q,

$$\frac{\Delta\Omega_2}{\Delta\Omega_1}\frac{\sum_{i\in M_1} R_i^3}{\sum_{j\in M_2} R_j^3} - q = 0\,, \tag{A9}$$

where $\Delta\Omega_1$ and $\Delta\Omega_2$ are the solid angles occupied by cones on M_1 and M_2, respectively.

The last equation is for the distance between the individual center of masses of the two bodies,

$$\frac{\sum_{i\in M_1}\cos(\phi_i)\sin(\theta_i)R_i^4/4}{\sum_{i\in M_1} R_i^3/3} - \frac{\sum_{j\in M_2}\cos(\phi_j)\sin(\theta_j)R_j^4/4}{\sum_{j\in M_2} R_j^3/3} = 0\,. \tag{A10}$$

To summarize, the set of equation to be solved can be written as $\vec{F} = 0$, where $\vec{F}$ is the $N_1 + N_2 + 2$ dimensional vector,

$$\vec{F}^{(N1+N2+2)} \equiv \begin{Bmatrix} \vec{F}^{(N_1)}_{j\in M_1} \\ \vec{F}^{(N_2)}_{j\in M_2} \\ F^{(1)}_q \\ F^{(1)}_d \end{Bmatrix} = \begin{Bmatrix} \sum_{i\in M_{1,2}} V_i(Rj) + V_{\rm rot}(R_j) + c_1 \\ \sum_{i\in M_{1,2}} V_i(Rj) + V_{\rm rot}(R_j) + c_2 \\ \text{Equation (A9) for the mass ratio} \\ \text{Equation (A10) for the separation} \end{Bmatrix} = 0\,. \tag{A11}$$

The upper parentheses denote the size of each vector.

In the numerical procedure, we start with an initial guess for the configurations, and iterate using a Newton–Raphson method (but see Appendix A.5), correcting the values of our variables $\vec{x} = (\vec{R}_{j\in M_1}, \vec{R}_{j\in M_2}, c_1, c_2)$ by $\vec{dx} = -\vec{F}\times\mathbf{J}^{-1}$, where $\mathbf{J}$ is the Jacobian derivatives matrix.

We compute the derivatives analytically. We iterate the Newton–Raphson scheme until the solution has converged, so that $\vec{F} = 0$ to within some numerical threshold, and the correction $\vec{dx}$ is small compared to $\vec{x}$.

A.4. Symmetry

As mentioned in Appendix A.1, we assume that the equilibrium configurations are symmetric about the $x-y$ and $x-z$ planes. We therefore distribute N points on the surface of a 1/4 sphere, between $\phi = 0$ and π, and between $\cos(\theta) = 1$ and 0.

When computing the potential produced by the i'th cone with orientation $(\mu_i = \cos(\theta_i), \phi_i)$, the contributions of the three symmetric cones at $(\mu_i, 2\pi - \phi_i)$, $(-\mu_i, \phi_i)$ and $(-\mu_i, 2\pi - \phi_i)$ must also be included.

The vector $\vec{F}$ therefore becomes,

$$\vec{F} = \sum_i [V_{R_i,\mu_i,\phi_i}(R_j) + V_{R_i,\mu_i,2\pi-\phi_i}(R_j) + V_{R_i,-\mu_i,\phi_i}(R_j) + V_{R_i,-\mu_i,2\pi-\phi_i}(R_j)] + V_{\rm rot}(R_j) + c = 0\,, \tag{A12}$$

and the Jacobian matrix $\mathbf{J}$ must be corrected accordingly to include the additional terms.

A.5. A Least Squares Newton–Raphson Solution

We find that the numerical efficiency is much increased if instead of using Equation (A10) for the distance between the center of masses, we use two equations,

$$\frac{\sum_{i\in M_1}\cos(\phi_i)\sin(\theta_i)R_i^4/4}{\sum_{i\in M_1} R_i^3/3} = 0, \tag{A13a}$$

$$\frac{\sum_{i\in M_2}\cos(\phi_i)\sin(\theta_i)R_i^4/4}{\sum_{i\in M_2} R_i^3/3} = 0. \tag{A13b}$$

We therefore solve an over-constrained problem, with $N1 + N2 + 3$ equations for $N_1 + N_2 + 2$ variables. We substitute the Newton–Raphson matrix division $\vec{dx} = -\vec{F}\times\mathbf{J}^{-1}$ with a so-called left-matrix division $\vec{dx} = -\vec{F}\backslash\mathbf{J}$, which is the solution, in the least squares sense, to the over-constrained system of equations, $\mathbf{J}\times\vec{dx} = -\vec{F}$. We use the values of $\vec{dx}$ derived using this modified Newton–Raphson scheme to correct the current solution, and iterate to convergence.

A.6. Numerical Accuracy

We consider the accuracy of our numerical method, as it applies to our best fit solution to the observed light curve of Kuiper Belt binary 2001 QG_{298}. This model has $q = 0.93$, $\Omega^2/G\rho = 0.333$, and $d = 2.8956$.

Given these parameters, we compare models constructed with various sampling resolutions, namely $N = 200, 400, 800, 1200$ and 1600 points on a quarter-sphere. We begin by estimating the "true" equilibrium configurations by extrapolating the functions $r_i(1/N)$ to $(1/N) = 0$ for each direction $i = 1\ldots N$. For each N we then compute the rms difference between the numerical solution and this "true" configuration, $\sqrt{\sum(R_{i,\rm sol} - R_{i,\rm true})^2/N}$, where $R_{i,\rm sol}$ are the distances from the center-of-mass to the surface in the numerical solution, and $R_{i,\rm true}$ are the distances from the center-of-mass to the surface in the extrapolated, "true" solution.

Since each solution is given at different azimuthal and polar angles, we first interpolate the center-to-surface distances of the high-resolution solutions onto the directions in which the lowest-resolution solution is known. We use these interpolated versions of the high-resolution solutions both to estimate the true configurations and to compute the rms differences.

Figure 15 shows our results for the rms difference versus the number of points. The filled symbols are for the more massive primary, and the empty symbols are for the lower mass companion. For example, the rms difference between the primary solution with 1600 points and the "true" solution is 0.0048. We note that the interpolation process introduces some errors that may increases this rms. These values can be compared with the rms difference between the numerical solution and the best fit ellipsoid (see Section 4.1 and Figure 5) which are 0.023 and 0.027 for the primary and companion, respectively.

APPENDIX B

COMPUTING LIGHT CURVES

B.1. Numerical Procedure

To compute the observed luminosity, we tile the surface of a given binary-configuration with triangles, typically two

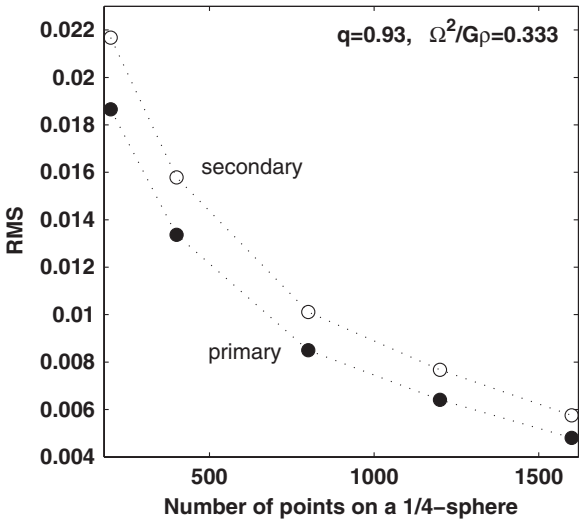

Figure 15. Example for the rms differences between "true" equilibrium configuration, and numerical solutions at different resolutions (see text). The horizontal axis shows the number of points on a quarter sphere. The filled symbols are for the more massive primary, and the empty symbols are for the lower mass companion.

triangles for each of the N points used when computing the equilibrium configuring. For the computations presented in Sections 3 and 4, which contain ∼1600 points on a quarter-sphere, this corresponds to ∼13,000 triangular tiles on each of the components.

We compute the x, y, z coordinates of the vertices of the triangular tiles. Given the orbital phase and inclination, we then rotate the coordinate system such that the positive z direction points toward the observer. Tiles with higher values of z are closer to the observer, and may block tiles with lower values of z from sight.

We now sort the tiles of both bodies according to their mean z values. For each tile, we compute the area projected on the x–y plane, A_i^{x-y}, and the angle between the normal to the tile surface and the Sun, ϑ_i.

We define a "visibility" function for each tile, V_i, describing the fraction of the tile's projected surface that is visible to the observer. For each tile, we estimate the visibility function by searching for other tiles that may block it from sight. We start with the tile closest to the observer (highest z value), and search for possible overlaps between its x–y position and the x–y positions of all the lower-z tiles. When an overlap exists, we reduce the visibility function of the lower tile, by an amount corresponding to the fraction of its area that overlaps with the higher tile, $V_i = V_i - A_{i,j}^{\rm overlap}/A_i^{x-y}$. We then repeat this procedure for every other tile, correcting the visibility of lower tiles.

This provides an *overestimate* of the reduction in visibility, since several high tiles may cover the *same* part of a lower tile, resulting in a "double-reduction" of the same covered area. This error remains small due to the simple shapes considered here.[9]

The total observed light is given by $\sum_i A_i^{x-y} \times V_i$ for the case of backscatter reflection, and by $\sum_i A_i^{x-y} \times V_i \times \cos(\vartheta_i)$ for the case of diffuse (Lambertian) reflection. To compute the light curve due to a given configuration viewed at a given inclination, this process must be repeated for a set of orbital phases between 0 and 2π.

[9] We verified that we obtain the correct projected area for the simple case of backscatter reflection from two spherical or elliptical components.

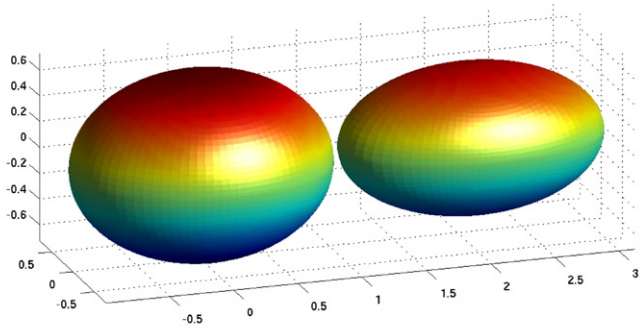

Figure 16. Configuration found by Takahashi & Ip (2004) for QG_{298}. (A color version of this figure is available in the online journal.)

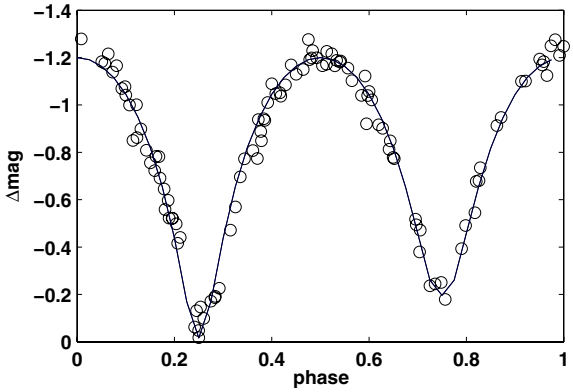

Figure 17. Light curve that we compute for the parameters inferred by Takahashi & Ip (2004). Compare to their Figure 2.

B.2. Sanity Checks

To verify the accuracy of our light-curve computations, we compared our models against published results for similar configurations. In particular, we focused on previous suggested models for QG_{298}. Two previous published models exist, both using the Roche ellipsoidal solutions. The first is by Takahashi & Ip (2004), and the second by Lacerda & Jewitt (2007).

According to Takahashi & Ip (2004), QG_{298} consists of two components with a mass ratio, $q = 0.65$. The primary has $e_1 = 0.61$ and $e_2 = 0.69$, and a secondary has $e_1 = 0.79$ and $e_2 = 0.83$. The separation is 2.1 times the primary's semi-major axis. The system is illustrated in Figure 16.

Takahashi & Ip find that their best fit indicates a ∼70% diffuse reflection plus ∼30% backscatter (uniform) reflection. For these parameters, they infer a bulk density of 0.63 ± 0.20 g cm^{-3}.

Figure 17 shows the light curve that we compute given the parameters inferred by Takahashi & Ip, along with the observed data points. A comparison of this light curve with that presented in Figure 2 of Takahashi & Ip, shows that our results are nicely consistent.

According to Lacerda & Jewitt (2007), QG_{298} is a binary with a mass ratio $q = 0.84$. Their primary has $e_1 = 0.69$ and $e_2 = 0.76$, and their secondary $e_1 = 0.89$ and $e_2 = 0.91$. The separation is 2.1 times the primary semimajor axis. This system is illustrated in Figure 18. Note that Lacerda & Jewitt accepted this configuration even though the two components overlap. They argue that they chose to accept it because of the inaccuracies imposed by the ellipsoidal and Keplerian nature of the Roche approximation, and due to our poor understanding of the formation mechanisms of such binaries.

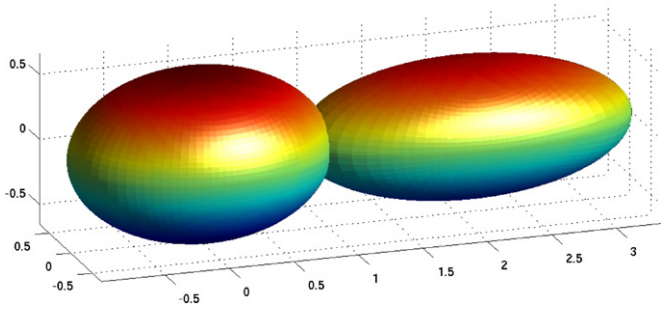

Figure 18. Configuration found by Lacerda & Jewitt (2007) for QG_{298}. (A color version of this figure is available in the online journal.)

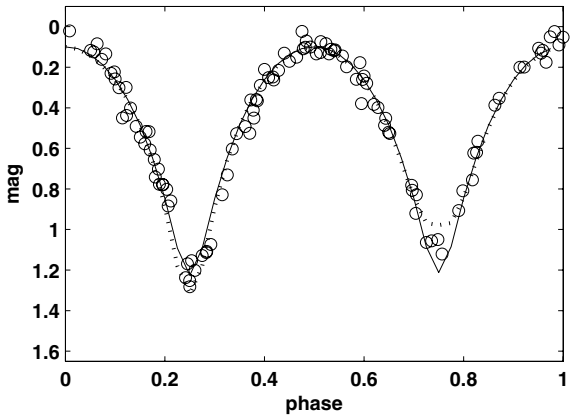

Figure 19. Light curve that we compute for the parameters inferred by Lacerda & Jewitt (2007). Compare to their Figure 9 (lower-left case). Here the solid curves are for backscatter reflection, and the dashed curves are for diffuse reflection.

Lacerda & Jewitt find that backscatter reflection best fits the observed light curve. These parameters indicate a bulk density of $0.590^{+0.143}_{-0.47}$ g cm^{-3}. In Figure 19, we display the light curve that we compute based on the parameters inferred by Lacerda & Jewitt (2007). Our light curves are again nicely consistent with those computed by Lacerda & Jewitt and shown in their Figure 9 (lower-left panel).

REFERENCES

Astakhov, S. A., Lee, E. A., & Farrelly, D. 2005, MNRAS, 360, 401
Cameron, A. G. W., & Ward, W. R. 1976, Lunar and Planetary Institute Science Conference Abstracts, 7, 120
Cellino, A., Pannunzio, R., Zappala, V., Farinella, P., & Paolicchi, P. 1985, A&A, 144, 355
Chandrasekhar, S. 1969, The Silliman Foundation Lectures (New Haven: Yale Univ. Press)
Darwin, G. H. 1906, Phil. Trans. R. Soc. Lond., 206, 161
Descamps, P. 2008, Planet. Space Sci., 56, 1839
Edgeworth, K. E. 1943, J. Br. Astron. Assoc., 53, 181
Farinella, P., Paolicchi, P., Tedesco, E. F., & Zappala, V. 1981, Icarus, 46, 114
Funato, Y., Makino, J., Hut, P., Kokubo, E., & Kinoshita, D. 2004, Nature, 427, 518
Gamboa Suárez, A., Hestroffer, D., & Farrelly, D. 2010, Celest. Mech. Dyn. Astron., 106, 245
Goldreich, P., & Sari, R. 2009, ApJ, 691, 54
Goldreich, P., Lithwick, Y., & Sari, R. 2002, Nature, 420, 643
Hachisu, I., & Eriguchi, Y. 1984a, PASJ, 36, 259
Hachisu, I., & Eriguchi, Y. 1984b, PASJ, 36, 239
Hartmann, W. K., & Davis, D. R. 1975, Icarus, 24, 504
Jacobi, C. G. J. 1834, Ann. Phys., 33, 229
Jewitt, D. C., & Sheppard, S. S. 2002, AJ, 123, 2110
Jewitt, D., & Luu, J. 1993, Nature, 362, 730
Kuiper, G. P. 1951, in 50th Anniversary of the Yerkes Observatory and Half a Century of Progress in Astrophysics, ed. J. A. Hynek (New York: McGraw-Hill), 357
Lacerda, P., & Jewitt, D. C. 2007, AJ, 133, 1393
Leone, G., Paolicchi, P., Farinella, P., & Zappala, V. 1984, A&A, 140, 265
Lee, E. A., Astakhov, S. A., & Farrelly, D. 2007, MNRAS, 379, 229
Luu, J. X., & Jewitt, D. C. 2002, ARA&A, 40, 63
McKinnon, W. B. 1989, ApJ, 344, L41
Naoz, S., Perets, H. B., & Ragozzine, D. 2010, arXiv:1001.2558
Noll, K. S., Grundy, W. M., Chiang, E. I., Margot, J.-L., & Kern, S. D. 2008a, The Solar. System Beyond Neptune, ed. M. A. Barucci et al. (Tucson, AZ: Univ. Arizona Press), 345
Noll, K. S., Grundy, W. M., Stephens, D. C., Levison, H. F., & Kern, S. D. 2008b, Icarus, 194, 758
Paul A. Abell, et al. (LSST Science Collaborations) 2009, LSST Science Book, Version 2.0, http://www.lsst.org/lsst/scibook
Perets, H. B., & Naoz, S. 2009, ApJ, 699, L17
Roche, M. (ed.). 1847, Acad. des Sci. de Montpellier, 1, 243
Schlichting, H. E., & Sari, R. 2008, ApJ, 673, 1218
Sheppard, S. S., & Jewitt, D. C. 2002, AJ, 124, 1757
Sheppard, S. S., & Jewitt, D. C. 2003, Earth Moon and Planets, 92, 207
Sheppard, S. S., & Jewitt, D. 2004, AJ, 127, 3023
Takahashi, S., & Ip, W.-H. 2004, PASJ, 56, 1099
Weidenschilling, S. J. 1980, Icarus, 44, 807
Weidenschilling, S. J. 2002, Icarus, 160, 212